Spring 2017

Geochronology Of Calc-Alkaline Ash Flow Tuff Units In The Ogollon Datil Volcanic Field, Southern New Mexico: U-Pb In Zircon

Shannon Porter Rentz

GEOCHRONOLOGY OF CALC-ALKALINE ASH FLOW TUFF UNITS IN THE MOGOLLON DATIL VOLCANIC FIELD, SOUTHERN NEW MEXICO: U-PB IN ZIRCON

A Masters Thesis

Presented to

The Graduate College of

Missouri State University

In Partial Fulfillment

Of the Requirements for the Degree

Master of Science, Geospatial Sciences in Geography, Geology & Planning

By

Shannon P. Rentz

May 2017

GEOCHRONOLOGY OF CALC-ALKALINE ASH FLOW TUFF UNITS IN THE MOGOLLON DATIL VOLCANIC FIELD, SOUTHERN NEW MEXICO: U-PB IN ZIRCON

Geography, Geology & Planning

Missouri State University, May 2017

Master of Science

Shannon P. Rentz

ABSTRACT

Caldera systems are capable of outputting voluminous quantities of volcaniclastic material with wide ranging negative environmental impacts. Determining the behaviors of previously erupted caldera systems may help inform predictive models used to evaluate hazards and assess risks for analogous currently active volcanic systems. The Mogollon-Datil volcanic field (MDVF) is a 40-24 Ma cluster of caldera activity in southern New Mexico tied to the subduction, and possible delamination, of the Farallon plate beneath the North American plate. A regional ignimbrite flare up from 36-24 Ma produced at least 28 caldera-forming eruptions. The calc-alkaline magmatism of three calderas in this field (the Mogollon, Bursum, and Gila Cliff Dwellings) produced several voluminous and regionally dispersed ash-flow tuffs. Magmatic zircon sampled from these tuffs record timescales of magmatic accumulation via U-Pb isotopic zonation. This study focuses on analysis of zircon crystals and the utilization of U-Pb isotope ratios as geochronometers for magmatic activity in the MDVF. I present new U-Pb geochronology results obtained via Sensitive High Resolution Ion Microprobe-Reverse Geometry (SHRIMP-RG) analysis of magmatic zircon from five MDVF ignimbrites. I compare previous geochronology results obtained via $^{40}Ar/^{39}Ar$ in sanidine to new U-Pb zircon age dates (1σ error), Pb isotopic ratios, and trace element compositions in the zircon samples.

KEYWORDS: zircon, geochronology, ignimbrite flare-up, MDVF, New Mexico

This abstract is approved as to form and content

_____

Gary S. Michelfelder
Chairperson, Advisory Committee
Missouri State University

GEOCHRONOLOGY OF CALC-ALKALINE ASH FLOW TUFF UNITS IN THE MOGOLLON DATIL VOLCANIC FIELD, SOUTHERN NEW MEXICO: U-PB IN ZIRCON

By

Shannon P. Rentz

A Masters Thesis
Submitted to the Graduate College
Of Missouri State University
In Partial Fulfillment of the Requirements
For the Degree of Master of Science, Geospatial Sciences in Geography, Geology & Planning

May 2017

Approved:

_____
Gary S. Michelfelder, PhD

_____
Kevin Mickus, PhD

_____
Matthew McKay, PhD

_____
Julie Masterson, PhD: Dean, Graduate College

ACKNOWLEDGEMENTS

I would like to thank the following people for their support during the course of my graduate studies: the faculty and staff of the Department of Geography, Geology and Planning at Missouri State University for their technical expertise and logistical support during this project. I thank Missouri State University undergraduates Eric Sikes, Brandie Oehring, and Ashley Gerik for their assistance in the field and in the lab. Funding for this project was provided by Missouri State University Graduate College and the Geological Society of America. I thank Dr. Frank Ramos for lab support at New Mexico State University, and Dr. Matt Coble for SHRIMP support at Stanford University. I would also like to thank Tyler J. Rentz, without whom I would never have arrived at all (TCOBIAMFF).

I dedicate this thesis to Michelle Fernung.

TABLE OF CONTENTS

LIST OF TABLES

LIST OF FIGURES

INTRODUCTION

Continental arc volcanic systems produce a compositionally and texturally wide range of rocks. These rocks often reflect the subsurface compositional diversity via explosive silicic volcanic products, such as the voluminous ignimbrites of the Andes stemming from the thick continental crust subducting the Nazca Plate (Kern et al., 2016; Kaiser et al., 2017). As is the case with any large scale magmatism, prior tectonic activity of the area controls the magma dynamics and composition of a volcanic system. In the case of the western North American plate, the non-collisional orogenic events of the Cretaceous leading into onset of Basin and Range extension dramatically shaped the crust through both compression and subsequent extension (Schneider and Keller, 1994; Seager, 2004). In southern New Mexico, the volcanic record between 80-20 Ma is an excellent cipher for underlying crustal transformations (McMillan, 2004). Throughout New Mexico, a regional ignimbrite flare-up from 36-24 Ma (Chapin et al., 2004) stemmed from the cessation of Farallon plate subduction and a possible lithospheric delamination (Farmer et al., 2007). Magmatic zircon can record timescales of magmatic accumulation via U-Pb isotopic zonation (Harley and Kelly, 2007; Kern et al., 2016). Zircon in ignimbrite, or other silicic volcanic products, can preserve a record of the magmatic processes that are too rapid to be represented in the plutonic record (Lipman, 2007; Wilson and Charlier, 2016) and serve as a snapshot in time during the accumulation and storage of a magmatic system (de Silva and Gosnold, 2007).

Previous work in the southern New Mexico volcanic fields often relied upon K/Ar and $^{40}Ar/^{39}Ar$ ages in biotite or sanidine, or zircon fission track ages for ages

of volcanic units (McIntosh et al., 1991). These data are interpreted as likely eruption ages for the volcanic rocks because the elemental or isotopic ratios best record the thermal cooling history of the minerals (McIntosh et al., 1991; Ramos et al., 2016). Alternatively, zircon geochronologic ages, based on the U-Pb series isotope ratios, are interpreted as the crystallization age of the zircon within the magmatic system (Watson and Harrison, 1983; Finch and Hanchar, 2003; Carricchi et al., 2016). The comparison of eruption ages from sanidine and U-Pb crystallization ages from zircon can give insight into the magmatic evolution of the Mogollon Datil Volcanic Field (McDowell et al., 2014; Carricchi et al., 2016; Deering et al., 2016; Kern et al., 2016; Kaiser et al., 2017).

The volcanic units analyzed here are rhyodacites through rhyolites erupted in the MDVF in New Mexico. Geochronologic data show zircon ages for these units ranging from 36.2-28.7 Ma. The time frame of this volcanic activity coincides with the regional ignimbrite flare-up described by Chapin et al. (2004) from 36-24 Ma. This study will address these models for the MDVF by looking at the geochemical evolution in a spatially restricted area over time.

In this study we present the combination of previous work in the MDVF (eruption ages, stratigraphic relationships, geophysical data showing crustal structure and likely location of the pluton related to MDVF volcanism (Ratté et al., 1984; McIntosh et al., 1992; Schneider and Keller, 1994) with new U-Pb geochronologic data and analysis to explore magmatic residence times. This study also addresses whether individual ash-flow tuffs of the MDVF are surface expressions of separate plutonic systems, or potentially sourced from a regional, mid-crustal intrusion.

GEOLOGIC BACKGROUND

Subduction of the Farallon plate widely influenced the tectonic and magmatic activity of the western United States between 80-37 Ma (Glazner and Ussler, 1989; Bowring and Karlstrom, 1990; Cather, 1990; McMillan 2004). The crustal shortening that resulted from tectonic contraction transitioned into crustal extension during the mid- to late-Tertiary as the Rio Grande rift and Basin and Range Province became active (Menard, 1978; Cather, 1990). Subduction of the Farallon plate is widely accepted as the cause of the continental arc-style magmatism throughout New Mexico and the Western North America (U.S.) between 80-37 Ma, the contemporaneous magmatism adjacent to the Sevier fold and thrust belt in the northern Rocky Mountains, and the magmatic gap ranging from northern New Mexico to southern Idaho (Seager, 2004; Gaschnig, 2010; Foster et al., 2012). Large-scale lithospheric mantle melting combined with crustal extension and thinning, triggered extensive explosive volcanic activity associated with the MDVF, the Southern Rocky Mountains Volcanic Field, and the Sierra Madre Occidental field in North America (Chapin et al., 2004; Farmer et al., 2007; Bachmann and Bergantz, 2008). This volcanism deposited thick, regionally extensive ignimbrite units throughout the southwest between 37-24 Ma, and thick andesite lava flows between 50-36 Ma.

Around 36 Ma, a geochemically and stratigraphically-abrupt shift from intermediate style magmatic activity to more bimodal basaltic andesite and rhyolitic composition volcanism occurred in southern New Mexico (Cather, 1990; McMillan, 1998). This is hypothesized to be a result of lithospheric delamination and slab roll back

of the Farallon plate and the transition from mafic magma generation via sub-lithospheric mantle melting to bimodal volcanism (Cather, 1990; McMillan, 1998; Farmer et al., 2007). In order to generate the volume of silicic magma necessary to produce the ignimbrite units present in southern New Mexico and southern Colorado (specifically the MDVF, and the San Juan volcanic field), there must have been systematic input (via lithospheric melting) of magma other than just subcontinental lithospheric mantle (Farmer et al., 2007.) The transition of principal stress directions caused by the cessation of subduction and the physical impact of the Pacific plate transform boundary provided a mechanism for a shift in the composition of the ignimbrite units from a high-calcium (Ca) plate margin type to an intra plate low-Ca variety at ~ 28 Ma (Elston, 2008). The regional dispersion of caldera activity displayed in New Mexico and Southern Colorado, extends from the San Juan Volcanic Field in Colorado and south to the Trans-Pecos Volcanic Field in the Sierra Madre Occidental in Mexico (Fig. 1). Within New Mexico itself, episodic pulses of volcanic activity began in the south near Las Cruces, New Mexico ~ 36.2 Ma and migrated northwest over a ~12 million year period (McIntosh et al., 1992).

The Mogollon-Datil Volcanic Field

Ignimbrite flare-up in southern New Mexico and Eastern Arizona followed a south to north trend parallel to that of the Rio Grande Rift. Punctuated volcanism stretched from the Sierra Madre Occidental in Mexico and Texas beginning at 45 Ma to the San Juan Volcanic Field in Colorado (Fig.1; Chapin et al., 2004). The styles of volcanism in southern New Mexico (Fig. 1) and the composition of the magmas erupted have changed significantly with the end of Laramide subduction through the initiation

and evolution of the Rio Grande Rift as a response to the change in tectonic regime (McMillan et al., 2000). In general, Laramide volcanism in the Basin and Range area including southern New Mexico, began with eruption of intermediate to silicic composition ignimbrites. These were followed by a period of syntectonic basin fill deposits as extension initiated and provides evidence to the timing of volcanism versus extension (Best and Christiansen, 1991; Gans and Bohrson, 1998). A decrease in extension rate and associated switch to alkali, dominantly mafic, volcanism in southern New Mexico resulted from an increase in crustal density and the intrusion of mafic magmas between 10-0 Ma (Glazner and Ussler, 1989; Thompson et al., 2005). The MDVF is an anomaly compared to ignimbrite flare-ups in other volcanic fields in that geophysical and petrological evidence for a regional scale magma reservoir (MASH zone; Hildreth and Moorebath, 1988; Annen et al., 2006) is lacking (Schneider and Keller, 1994). Competing models for ignimbrite flare-up and crustal magma accumulation suggest that either large magma reservoirs only contain a small percent eruptible melt (Glazner et al., 2004) or more punctuated intrusion where ignimbrites only erupt at the peak of intrusion (de Silva and Gosnold, 2007). Comparison between volcanic and plutonic components (where exposed) of a magmatic system can show petrologic and geochemical evidence of melt processes (fractional crystallization, remobilization, chemical evolution; Zimmerer and McIntosh, 2013; McDowell et al., 2014). The extension from the Rio Grande Rift activity exposed the plutonic components of magmatic systems in many areas of New Mexico (e.g., the Organ Needle Pluton; Zimmerer and McIntosh, 2013), but the proposed source plutons for MDVF volcanic

centers remain unexposed at the boundary between the Colorado Plateau and the Basin and Range provinces (Schneider and Keller, 1994).

The broadly categorized rocks in the MDVF are separated into distinct time periods of magmatism based upon Ar^{40}/Ar^{39} age distribution (Davis and Hawkesworth, 1995). These time periods, also referred to as volcanic 'pulses' by McIntosh et al. (1992), are (1) 36.2-33.5 Ma: First Flare-Up, (2) 32.1-31.4 Ma: Short Burst, (3) 29.0-27.4 Ma: Big Doublet, and (4) 26.1-24.3 Ma: Last Gasps. Each pulse is separated by a ~ 2 Ma period of quiescence (McIntosh et al., 1992). To the north of the MDVF, episodic volcanism also occurred in the San Juan Volcanic Field (Fig. 1) beginning with a waxing stage at ~35 Ma, progressing to an ignimbrite producing stage at ~29 Ma, and followed by a waning in volcanism at ~ 14 Ma (Lipman, 2007).

Ignimbrites of the Mogollon Datil Volcanic Field

The dynamic crustal situation beneath the MDVF during ignimbrite flare-up makes the geologic units presented in this study particularly diagnostic. The MDVF ignimbrites represent the surface expression of the transition from Farallon plate subduction through crustal delamination to asthenospheric mantle input (Menard, 1978; McMillan, 1998; 2004; McMillan et al., 2000; Farmer et al., 2007). The early Oligocene Bell Top rhyolite tuff marks an abrupt transition in the style and composition of volcanism in the MDVF (McMillan, 2004). This bookend ignimbrite corresponds to the cessation of subduction in the western United States/initiation of regional rifting, and initiated the "First Flare-Up" designated by McIntosh et al. (1992). This unit is followed in the west (Fig. 2) by the Cooney Formation, a lower Oligocene/upper Miocene rhyolite

to quartz latite ash-flow. The Cooney Formation is the oldest exposed caldera forming sequence in the Mogollon Range (Ratté, 2006). The 2nd pulse units are only exposed in the north of the MDVF, west of Socorro, New Mexico and north of Winston, New Mexico. The Shelley Peak and Davis Canyon tuffs (both rhyolitic ash-flow tuffs) are members of the 3rd magmatic pulse (the largest in the field, known as the "Big Doublet"; McIntosh et al., 1992) in the MDVF. The Davis Canyon tuff was the first regional ignimbrite (>10,500km^2) erupted in the 3rd pulse after a ~ 2 million year period of quiescence in the south MDVF (McIntosh, et al., 1992). The Shelley Peak tuff is the youngest exposed volcanic product of the Gila Cliff Dwellings caldera (Ratté et al., 1984; McIntosh et al., 1991). The Shelley Peak is stratigraphically controlled by the overlying Bloodgood Canyon tuff, and marks the transition from Gila Cliff Dwellings caldera activity to the initiation of the Bursum caldera activity (Ratté et al., 1984). Together, these units represent important time slices within the overall magmatic context of volcanism in the MDVF.

Bell Top Tuff. The Bell Top Formation (35.7 to 28.5 Ma; McIntosh et al., 1991; 1992) consists of 6 high-K, calc-alkaline dacite to rhyolite ash-flow tuffs (numbered 2-7) of uncertain caldera origin that are exposed in the Sierra de las Uvas volcanic field (Fig. 2; Mack et al., 1994). The formation is topographically controlled by the Goodsight-Cedar Hills depression, and fills the depression at a maximum thickness of 550 meters (Seager, 1975). The Bell Top Formation is interbedded with 165 m^3 of epiclastic deposits, and capped by Oligocene to early Miocene basaltic andesite. It unconformable overlies the Rubio Peak formation in the Goodsight Mountains and the Palm Park

Formation elsewhere (Mack et al., 1994). The Bell Top 4 tuff (hereafter referred to as the Bell Top tuff) is 3-55 m thick over an area of ~3000 km^2. The Bell Top tuff contains abundant, characteristically large (≥ 1 foot) pumice clasts. Phenocrysts include ~ 15% euhedral to subhedral sanidine and plagioclase in a densely welded and devitrified matrix with <1% oxidized biotite and quartz (Clemons, 1975). Some plagioclase feldspar phenocrysts show resorption textures. The eruption age for the Bell Top tuff is 34.9 ±0.04 Ma (McIntosh et al, 1992).

Cooney Formation. The members of the Cooney Formation members are late Eocene to early Oligocene (~34 Ma; McIntosh et al., 1992) quartz latite ash-flows and ash-fall units exposed in and around the Mogollon mining district in western New Mexico (Fig.2). Total exposed formation thickness is ~1000 m (Ratté et al., 2006). The three recognized members of the Cooney Formation are the South Fork tuff, the Whitewater Creek tuff, and the Cooney Canyon tuff.

The South Fork member has a limited outcrop exposure that is restricted to the front of the Mogollon Range at the intersection with the mouth of the Whitewater Canyon. There are five 10-65 m thick mafic lava flows interbedded with multiple partially- to densely-welded ash-flows in the South Fork member. Phenocryst character and content is similar to the Cooney Canyon member (Ratté et al., 2006). There ~2% pervasively altered, often bright green, 0.5-2 cm elongated pumice clasts. Total unit thickness, including mafic lavas, is 400-500 m. These tuffs are highly altered, and no fresh material was observed.

The Whitewater Creek member is a 100-200 m thick, crystal-poor, single cooling unit, densely to partially welded ash flow tuff with <1% plagioclase feldspar, biotite, and quartz phenocrysts. Sparse lithic clasts (< 20 cm) vary throughout the unit. There is some evidence of post-depositional rheomorphic flow structures. Three characteristic zones distinguish the Whitewater Creek member; a base lithophysal zone grades into a second zone with columnar-jointing, and topped with a planar, foliated zone (Ratté, 1981; Ratté et al., 2006).

The Cooney Canyon member is comprised of multiple cooling units of ash-flow tuff with ~500 m of thickness. The stratigraphically lowest tuffs of the unit contain at least 5 discontinuous, well-sorted, 0-10 m thick volcaniclastic conglomerate beds. The phenocryst content varies from 10-30% and phenocrysts include 1-3 mm sodic plagioclase, biotite, and opaque Ti-Fe-oxides in densely- to poorly-welded groundmass (Ratté et al., 2006).

Davis Canyon Tuff. The Davis Canyon tuff is a 200-400 km^3 high-silica rhyolite ash-flow tuff with a regional thickness of 0-150 m, and an extent of >10,500 km^2 (McIntosh et al., 1992). The tuff outflow sheet is best preserved in the wall of the Bursum caldera. In outcrop, the Davis Canyon appears blue to light grey. It is phenocryst-poor, with 1-10% sanidine, quartz, and sodic plagioclase that range from micro-phenocrysts to >1 mm. The Davis Canyon tuff is multiple partially- to densely-welded cooling units with >10cm brown or gray eutaxitic pumice throughout (Ratté et al., 1981). Pumice may range up to 20 cm long and show lineation in some locations (Finnell and Ratté, 2006).

Shelley Peak Tuff. The Shelley Peak tuff is a 100-200 km^3 (McIntosh et al., 1992) crystal-rich, compositionally zoned rhyolite ash-flow tuff, locally 50-200 m thick. The source of this unit was initially unknown (Ratté, 1981) but was later attributed to the Gila Cliff Dwellings caldera (Ratté et al., 1984). This outflow tuff is also preserved as a fragment in the wall of the Bursum caldera structure. The contact between the Shelley Peak and the Davis Canyon is delineated by rhyolitic tuff breccia and other volcaniclastic rocks in the north, but directly uncomformably overlies the Davis Canyon tuff in the Mogollon area. The Shelley Peak is overlain in most areas by the Bloodgood Canyon tuff, and separated by an erosional unconformity and ~1-10 m cross-bedded, conglomeratic sandstone (Ratté, 1981). This tuff has a distinctive brick-red groundmass. Phenocryst content is 10-40% sodic plagioclase and sanidine, with 1-2% green clinopyroxene, accessory zircon and biotite (Ratté et al., 1981).

Other MDVF Ignimbrites. Although not specifically discussed in this paper, the volcanic output of the adjacent Bursum caldera provides additional data for and constraints on the models used to describe magmatic activity in the MDVF. Contemporaneous to the output of the Gila Cliff Dwellings caldera are these ash-flow units: the Fanney rhyolite (26.4-24.4 Ma), the Bloodgood Canyon tuff (28.0 Ma), and the Apache Spring tuff (27.9 Ma; Ratté et al., 1984; Bickerman et al., 1992). The age relationships between these Bursum-sourced units are established via stratigraphic evidence and age dating because the caldera itself collapsed, and only a few presumed structural wall fragments are preserved (Ratté, 1981; 2006). The Bursum caldera may

have erupted ~1200 km^3-2500 km^3 of magma prior to dome resurgence (Ratté et al., 1984).

The Bloodgood Canyon tuff (BCT) is a single cooling unit of compositionally zoned, high-silica rhyolite ash-flow tuff that extends over a 15,000 km^2 area with a minimum thickness of 600 m, and a volume of 1200 m^3 (Ratté, 1981; Ratté et al., 1984). The BCT uncomformably overlies the Shelley Peak and Davis Canyon tuffs proximal to the inferred Bursum caldera margin (Fig. 2). Lithic fragments at the base of the tuff contain pumice from both the Shelley Peak and Davis Canyon tuffs (Salings, 2017).

Geochemistry of the MDVF. Geochemically, the rocks in the MDVF may be separated into three time periods of magmatism (Davis and Hawkesworth, 1995). The pre-30 Ma and 30-20 Ma rocks are calk-alkaline, and show $^{87}Sr/^{86}Sr$ and $^{143}Nd/^{144}Nd$ isotope enrichment and possible derivation from lithospheric mantle (Davis and Hawkesworth, 1995). Post-20 Ma rocks in this area show compositional similarity to an oceanic island basalt (OIB) type isotopic ratios, and therefore are likely asthenospheric in origin (Bickerman et al., 1989; Davis and Hawkesworth, 1995; McMillan et al., 2000). Bickerman (1994) elaborates on these isotopic trends in the Davis Canyon and Shelley Peak ignimbrites. The $^{87}Sr/^{86}Sr$ ratios in these two units are essentially identical, pointing toward a more compositionally primitive magma source than the Bloodgood Canyon tuff (Salings, 2017). Based on field relationships and other geochemical evidence, Bickerman (1994) suggests that the Shelley Peak and Davis Canyon are products of the same magma chamber. The Davis Canyon and Shelley Peak units have a lower $^{87}Sr/^{86}Sr$ ratio than the

Bloodgood Canyon tuff, which Bickerman (1994) attributes to longer residence time in the chamber, and/or increased contact with contaminated country rock.

The previously determined $^{87}Sr/^{86}Sr$ ratios for the Cooney Formation, Shelley Peak, and Davis Canyon are similar to those in modern volcanic arc settings (0.703-0.716; Bickerman, 1989), supporting the hypothesis of decreasing crustal (cratonic) input via contamination or melting into the system through time. Geochemical modeling of Gila Cliff Dwelling caldera products supports the hypothesis of a mixed, rhyolitic magma chamber fractionating out 80:20 plagioclase feldspar to clinopyroxene (Bickerman et al., 1992; Bickerman, 1994). This is supported petrographically by the presence of clinopyroxene in the Shelley Peak tuff (Bickerman, 1994). $^{143}Nd/^{144}Nd$ and $^{87}Sr/^{86}Sr$ ratios and AFC modeling suggest magmatic activity from the Gila Cliff Dwellings and subsequent Bursum caldera may also be the product of primary mantle-derived magma and some crustal component mixing (Bickerman et al., 1992; Salings, 2017).

Petrological, geochemical, and geophysical evidence indicate remobilization of a closed system crystal mush as an eruptive trigger for the explosive volcanic episodes of the Gila Cliff Dwellings and Bursum calderas (Salings, 2017). A two-dimensional refraction model has shown the Moho to deepen abruptly about 90 km north of Silver City (from 34 to 37 km depth; Schneider and Keller, 1994) and imaged a low-velocity body in the mid-crust. Two-dimensional gravity modelling provided additional constraints on the existence of the low density body. The body was initially found by the seismic survey. The low-density body roughly coincides with the N/S mid-point of the crustal thickening (crossing the border from New Mexico to Arizona). This body is

interpreted as the underlying granitic pluton that possibly fed the voluminous mid-Tertiary volcanics in the MDVF (Ratté et al., 1984; Schneider and Keller, 1994).

Record of Volcanism in the MDVF

The MDVF activity covered an estimated 40,000 km^2 and was active from ~ 40 to 24 Ma (McIntosh et al., 1992). The 12,000km^3 of volcanic arc output manifested in several pulses of high-K, calc-alkaline, compositionally bimodal ignimbrites and small volume lava flows (Elston et al., 1970; McIntosh et al., 1992; Davis and Hawkesworth, 1994). The volcanic structures of the MDVF may be divided along a roughly north-south axis (termed the Santa Rita-Hanover axis) created by the structural and topographic high point of the Cretaceous Santa Rita volcanic stock (Elston et al, 1970). This high point constrained the emplacement of the ash-flow tuffs erupted to the east and west prior to the onset of extensional faulting. The three calderas that are within the western MDVF during the time period of interest are discussed below (Table 1).

Part of the first regional magmatic pulse in the southwest MDVF, the oldest ignimbrites in this suite, dated via K-Ar at 35.5-33 Ma (Bickerman, 1989) are the three members of the Cooney Formation (Fig. 2). The oldest members, the Whitewater Creek and South Fork tuffs, as well as the younger Cooney tuff are mapped largely as undifferentiated within the Mogollon, N.M. area (Ratté, 1981). These units are identified as the explosive intracaldera fill of the Mogollon caldera (Ratté et al., 1984). Outflow sheet exposure was identified by Ratté et al. (2006) at one location in the Big Lue Mountains of Arizona.

Overlying the Cooney Formation are ignimbrites suggested to have subsequently erupted from the Gila Cliff Dwellings caldera during the 3rd magmatic pulse (McIntosh, et al., 1992; Ratté et al., 1984). These outflow units consist of the stratigraphically-lower Davis Canyon tuff (29.3-29.0 Ma; Bickerman, 1989), and the Shelley Peak tuff (28.2 Ma; Bickerman, 1989; McIntosh et al., 1992) ash-flows are interspersed with volcaniclastic sandstone units and represent multiple events prior to caldera collapse.

ZIRCON AS A GEOCHRONOMETER

This study uses zircon crystals and U-Pb isotope ratios as a geochronometer for the magmatic system evolution in the MDVF. The preferential incorporation of uranium into the crystal lattice (due to high partition coefficient), the exclusion of lead form the lattice (due to low partition coefficient), as well as the ubiquity of zircon mineral phases in rhyolitic composition magmas allow for the ready use of zircon in comparative geochronological analyses (Mahood and Hildreth, 1983; Miller and Wooden, 2004; Kern et al., 2016). Zircon closure temperatures are well above critical felsic magmatic crystallization temperatures at ~800°C (Finch and Hanchar, 2003; Miller et al., 2003; Miller and Wooden, 2004), so the distribution of rare earth elements and isotopic ratios within a zircon crystal may reasonably be used as a proxy for melt crystallinity and magma composition (Hanchar and van Westrenen, 2007; Smith et al., 2009; Wotzlaw et al., 2013; McDowell et al., 2014; Bucholtz et al., 2017; Kaiser et al., 2017).

In silicic magmatic environments, the comparative rapidity of volcanic processes (versus plutonic) renders their quenched volcanic products useful diagnostic "snapshots" of melt composition at the time of eruption (de Silva and Gosnold, 2007; Wilson and Charlier, 2016). The U/Pb ratios within zircon crystals are not affected by high-temperature residence within the magma reservoir; provided the melt stays above the zircon saturation composition and appropriate temperature (Watson and Harrison, 1983; Hanchar and Watson, 2003). Crystal growth will therefore preferentially include U and exclude Pb in each subsequent growth zone in equilibrium with changes in magma composition and providing a tool to estimate residence in the system (Hanchar and

Watson, 2003). The $^{238}U/^{206}Pb$ is the most appropriate decay chain to analyze for volcanic rocks older than 150 Ka due to the accurately measurable quantity of ^{206}Pb present by that age (Hanchar and Watson, 2003). Other U-Pb isotopic concentrations are measured (i.e., $^{207}Pb/^{206}Pb$, $^{208}Pb/^{232}Th$) to evaluate age concordance between all results, and ensure accuracy of calculated age dates. Trace element composition of igneous zircon, particularly U, Th, Hf and Y combined with HREE abundance can be used to interpret and contextualize isotopic age date results (Hoskin and Schaltegger, 2003; Smith et al., 2009; Kaiser et al., 2017).

METHODS

Sample Collection and Preparation

Bulk whole rock samples from the Cooney formation members, the Shelley Peak and Davis Canyon tuffs were collected from around the Mogollon, N.M. area. Distal samples were also collected from near Clifton, Arizona and Luna, N.M. (Fig. 2). These units represent the span of the regional ignimbrite flare-up in the MDVF, ranging from onset to peak eruptive output in the western MDVF. The Arizona location is identified as potential outflow sheet from the Gila Cliff Dwellings caldera. All other units are identified as intracaldera fill. Sample location selection was based on proximity to the remnants of the Mogollon caldera structure, the type section for the Cooney formation, and the locations of samples taken for previous $^{40}Ar/^{39}Ar$ analysis (McIntosh et al., 1991). When available, zircon from within pumice was analyzed to avoid foreign crystal contaminants from wall rock interaction during eruption or incorporation of lithic zircon during emplacement.

Zircons for analysis were separated from bulk rock samples using standard techniques. Samples were mechanically separated via crushing and sieving. The >200μ fraction was first magnetically separated through Frantz processing at ~1.8A and 10˚ side slope to remove high-U zircon that might give discordant and unreliable results (Rosenblum, 1958; Sircombe and Stern, 2002). The remainder was processed through heavy liquids separation using Lithium Sodium Polytungstate. Optical picking ensured pure separates.

Approximately 75-100 grains were mounted in epoxy, cured, and manually ground to expose zircon grain interiors to present an even surface for analysis. The grain mounts were then polished, and imaged by cathodoluminesence and backscatter electron imaging to ensure analysis of zircon over other similar phases. The images were used to create composite grain mount maps and program analyses.

U-Pb Sensitive High Resolution Ion Microprobe-Reverse Geometry Analysis

U-Pb isotope ratios and trace element compositions within zircon were obtained via Sensitive High Resolution Ion Microprobe-Reverse Geometry Analysis (SHRIMP-RG) at the Stanford University Microscopic Analytical Center. Analytical procedures followed Strauss et al. (2016). 52 spot analyses were performed on 48 individual grains from 5 different pyroclastic ash-flow units (The Bell Top tuff (sample # UV-R2), the Whitewater Creek tuff (sample # CC-02), the Cooney Canyon tuff (sample # MO-09), the Shelley Peak (sample #180-SP-1), and the Davis Canyon tuff (sample # 78-1)).

Scanning electron microscope cathodoluminescence imaging (Fig. 3) at 15kv was utilized on mounted grains to select high uranium oscillatory targets for SHRIMP-RG analysis. Complex or altered cores were avoided. Where crystal size permitted or obvious zoning was present, both rim and core compositions within a single grain were analyzed.

SHRIMP-RG results were corrected for analytical drift using the SHRIMP-RG lab Temora-2 analytical age standard for U-Pb isotopic composition, and reduced using the SQUID 2.51.12.07.22, rev. 22 Jul 2012 software program (Ludwig, 2009). All U-Pb ages are reported with a 1σ uncertainty (95% confidence, unless otherwise noted) using the TuffZirc algorithm in Isoplot 4.15 (Ludwig, 2008).

Zircon Trace Element Analysis by SHRIMP-RG

All zircons analyzed for U-Pb ages were simultaneously analyzed for trace element composition including Fe, Y, Hf, and rare earth elements (La, Ce, Nd, Sm, Eu, Gd, Dy, Er, and Yb) at the SHRIMP-RG lab. Analytical standards were the same as used for U/Pb. Ti^{48} and Ti^{49} isotopic concentrations were also measured to monitor for analytical drift.

RESULTS

Zircon Trace Element Geochemistry

The zircon trace element distribution of the MDVF ignimbrite samples compared to global environments and tectonic regimes (Carley et al., 2014) is illustrated in Figure 4 and is presented in Table 2. All of the samples fall within the continental arc field values except for the MORB-like values of Sample 78-1 in U/Yb vs Y. The distribution of results within the continental arc field is similar for the U vs Yb values and U/Yb vs Hf, again with the exception of the borderline MORB-like cluster of zircons from Sample 78-1 for U vs Yb. Anomalously high Fe compositions (> one order of magnitude difference from average population composition) could be an indicator of secondary alteration or inclusions. As such, spot results that fell outside the average range of compositions were excluded from consideration.

Further information about melt extraction and duration may be inferred from the Y/Dy ratio results. Most of the ash-flow zircon plot with a <15 Y/Dy ratio (Fig. 5a), but there is a distinct population with ratios >15. These outliers are the rim (+1 single crystal) from ash-flow unit (180-SP-1) shown in Figure 5b.

During crystallization and remelting, slight changes in the trace element budget of a melt are reflected in the crystallized zircon. Extreme compatibility of trace elements into titanite can be a controlling factor on the concentrations and ratios thereof in the residual melt. Most of the samples have Yb/Dy ratios ranging from 2.5-6 (Fig. 6), except for the distinct cluster of rims from 180-SP-1 that are all >8. A complementary comparison, Th/U ratios in zircon can model temperature influence on the melt system

(Wotzlaw et al., 2013). An increase in Th/U usually reflects a sympathetic increase in melt temperature. MDVF ash-flows do not show any obvious correlation between Th/U (Fig. 7a) and Yb/Dy ratios (Fig. 7b).

Feldspar fractionation, crystallization and stability in the magmatic source can be traced via Eu/Eu* ratios (shown vs Hf in Fig. 8). Samples 180-SP-1(the Shelley Peak tuff; Eu/Eu* = 0.17 to 12.62) and UV-R2 (the Bell Top tuff; Eu/Eu* = 0.86 to 7.16) show a negative linear trend with increasing Hf (Fig. 9). The Cooney formation members (Eu/Eu* = 0.73 to 12.70) and Sample 78-1 (Eu/Eu* = 1.97 to 12.43) show no correlation across Eu/Eu* ratios and Hf compositions.

The concentration of Ti in igneous zircon has been suggested to correlate to melt temperatures (Watson and Harrison, 2005). With the mineralogical context of SiO_2 and TiO_2 behaviors included, Ti concentration evolves into a thermometry tool (Ferry and Watson, 2007). Figure 6 shows the WMDVF results as Hf vs. Ti (˚C temperature calculated via task equation after Strauss et al., 2016). Hf and temperature show an inversely correlated linear relationship, and as such Hf concentration may be used as a proxy for melt temperature at time of crystallization (Deering et al., 2016). The distribution of Hf concentration vs. Sm/Yb shows two distinct fractionation trends (Fig. 8). The first trend has a flat Hf content with variable Sm/Yb ratios, which has been suggested to represent amphibole/pyroxene dominated fractionation in the melt. The second trend is an inverse linear relationship between increasing Hf content and decreasing Sm/Yb ratios. This trend suggests apatite/titanite dominated fractionation in the melt, as apatite and titanite preferentially incorporate Sm to Yb (Kd_{Sm} = 17.7, Kd_{Yb} = 564; Mahood and Hildreth, 1983) into the crystal lattice during crystallization.

Rare Earth Elements (REEs)

Chondrite normalized REE trends for all units are given in Figure 11. UV-R2 has a several order of magnitude dispersion for the LREEs (light rare earth elements), the spread persists through middle REEs, and coalesces in the HREEs. The trend for one analysis differs in the Eu anomaly. CC-02 has a smaller discrepancy in the LREEs, but still several orders of magnitude separating the population. Overall, the trends are consistent throughout this unit. MO-09 has two orders of magnitude separation in the LREEs, and maintains that discrepancy through the entire REE series. There is an anomaly (the 1109 Ma ±18 xenocryst) that has a much greater Eu anomaly than any of the other zircon in this sample population. 180-SP-1 has two distinct populations with opposite trends through the LREEs, similar plateaus through the mid-REEs, and again opposite trends into the HREEs. The results are separated into core and rim distinctions in Figure 12a. The distinction between core and rim for sample UV-R2 (Fig. 12b) lies in a few orders of magnitude in concentration, with similar trend slopes.

U-Pb Zircon Ages

Zircon morphology. New U-Pb zircon data from MDVF ash-flow tuffs is presented in Table 3 and illustrated in Figure 13. Five samples were dated at the Stanford University SHRIMP-RG lab, and additional ages are from Michelfelder and McMillan (2012), Zimmerer and McIntosh (2013), and Deering, et al. (2016). New zircon crystals from this study in all units ranged from 75 – 300 μm (Fig. 3). The UV-R2 (Bell Top tuff 4) grains were mostly sub- to euhedral and elongate (Fig. 3d). Most grains also show some evidence of resorption. The Cooney formation units displayed some morphological

differences between units. The Whitewater member (CC-02) zircon grains were largely equigranular and euhedral, with local intermediate rim resorption textures in most grains, core resorption textures in ~ half of the grains, and clear overgrowths in ~ 2 grains (Fig. 3b). In contrast, the Cooney Canyon member (MO-09) zircons were largely elongate with a greater degree of core resorption characteristics than the Whitewater zircons (Fig. 3a). The 78-1 (Davis Canyon age tuff) zircons were euhedral with a variety of crystal morphologies, and lacked resorption textures in the majority of the grains (Fig. 3e). The Shelley Peak tuff (180-SP-1) zircons showed equigranular euhedral morphology in most grains, with resorption textures in most cores (Fig. 3 c, f). Zircon textural and resorption designations are based on Corfu et al. (2003).

Zircon Age Dates. Probability density function (PDF) curves from MDVF samples 180-SP-1, UV-R2, MO-09, and CC-02 (Fig. 13) all show zircon age crystallization peaks millions to thousands of years prior to eruption dates. The PDF peaks represent the greatest density of zircon ages within the sample populations. Sample 78-1 has an eruption age of 29.01 Ma that pre-dates the peak of zircon crystallization (Fig. 12), but is within the 1σ error reported for the $^{40}Ar/^{39}Ar$ age of the Davis Canyon tuff (McIntosh et al., 1992) late-stage crystallization and eruption are age concordant. From a sample population of 52 spot analyses, 8 analyses from 4 units were excluded from the within unit age calculations for variance too far from the $^{206}Pb/^{238}U$ weighted mean for each unit (2 younger than the mean, and 6 older).

Where crystal size allowed, analysis of both core and rim locations were performed (Fig. 3). Most rim and core analyses on the same crystal were statistically indistinguishable, with the exception of a core analysis on 78-1 (spot 3.2) that had an

outside of weighted mean age older than the population. Interior ages in most zircon pre-dated the exterior zones of the crystals by 10s - 100s Ka.

The youngest zircon ages (Fig. 13) overlap with the $^{40}Ar/^{39}Ar$ ages (uncertainty included) in all units, except for one analysis in 180-SP-1 and one analysis in 78-1. The amount of overlap between zircon crystallization and interpreted eruption dates varies among ash-flow units. For UV-R2, MO-09, and CC-02, the youngest zircon ages coincide with the eruption age. For samples 180-SP-1 and 78-1 the eruption age is only within error of the youngest zircon age. The $^{206}Pb/^{238}U$ weighted mean age result, when compared to the $^{40}Ar/^{39}Ar$ age result (Table 3), shows zircon crystallization timescales of thousands to millions of years.

This sample population did not present any significant anomalies between the weighted mean zircon age result for each unit and the $^{40}Ar/^{39}Ar$ age in sanidine for each unit. All variations were within error of the age results. The Bell Top tuff zircons yielded a U-Pb age range of 31.6 ±3 to 36.4 ±1 Ma, when compared to the $^{40}Ar/^{39}Ar$ age of 34.96 Ma yielded a residence time estimate of 0.04 Ma. The Whitewater Creek tuff zircons yielded a U-Pb age range of 33.9 ±2 to 37.2 ±1 Ma, when compared to the $^{40}Ar/^{39}Ar$ age of 34 Ma yielded a residence time estimate of 2.2 Ma. The Cooney Canyon tuff zircons yielded a U-Pb age range of 34.1 ±1 to 35.7 ±1 Ma, when compared to the $^{40}Ar/^{39}Ar$ age of 34 Ma yielded a residence time estimate of 0.8 Ma. The Davis Canyon tuff-age zircons yielded a U-Pb age range of 27.2 ±3 to 30.9 ±1 Ma, when compared to the $^{40}Ar/^{39}Ar$ age of 29.01 Ma yielded a residence time estimate of 0.19 Ma. The Shelley Peak tuff zircons yielded a U-Pb age range of 27.5 ±1 to 30.7 ±2 Ma, when compared to the $^{40}Ar/^{39}Ar$ age of 28.1 Ma yielded a residence time estimate of 1.5 Ma.

Xenocrysts

A zircon U-Pb age date of > 50 Ma is considered to be xenocrystic within the sample populations of the ash-flow tuffs presented here. The relative absence of xenocrystic zircons within the sample populations (i.e., 1 spot analysis yielding an age date of 1109 Ma ±18 from sample MO-09) suggests either a limited interaction between the source magma reservoir and other magmatic influences, or temperatures above the zircon crystallization range and changing magmatic compositions within the reservoir conducive to total zircon resorption. However, the number of xenocrystic cores may be biased based on the number of grains analyzed per sample and the relatively high number of xenocrystic zircons reported by Michelfelder and McMillan (2012) for intermediate ash-flows of similar age in the eastern section of the MDVF.

DISCUSSION

For the western MDVF ignimbrites, individual U-Pb zircon crystal age results are interpreted as an indication that there was zircon saturated melt present in the system at that time. Zircon autocryst age dates are used here to constrain the history of the pre-eruptive magmatic system by examination of how magmatic compositions vary through time (Kern et al., 2016). The weighted mean age of all the individual spot analyses for each unit is interpreted as the zircon crystallization age (Caricchi et al., 2016; Deering et al., 2016; Kern et al., 2016). The U-Pb age dates are not unique results, and should be considered within geologic context for interpretation and to explore magmatic residence times. Xenocrystic zircon are sourced from outside the magmatic system, and therefore are not related to or representative of magmatic conditions that produced the autocrysts (Kern et al., 2016). The presence of xenocrysts does suggest some limited interaction with the crustal country rock, and a small amount of assimilation into the magmatic system (Deering et al., 2016).

U-Pb Ages of Autocrysts Reveal Magmatic Age of MDVF Ignimbrites and Model Duration of Zircon Crystallization

The zircon populations for all five units analyzed have mean squared weighted distance (MSWD) values that are within 95% confidence. Within individual units, 8 total spot analyses were not considered in the age calculations due to dispersion beyond the confidence interval. For the Cooney Formation and Shelley Peak tuff, the zircon autocryst ages are distinctly older than the eruption age (Fig. 14). This suggests that

zircon growth in the magmatic system occurred prior to eruption indicating that the magmatic conditions were conducive to zircon crystallization for the duration of the residence period. All units show some overlap between magmatic ages and eruption ages (Fig.13) which is attributed to the error in the $^{40}Ar/^{39}Ar$ analyses. The Bell Top tuff shows a greater dispersion of ages, but the majority of the population still overlaps the $^{40}Ar/^{39}Ar$ eruption age within error. The Davis Canyon-age tuff had a larger population of analyses fall outside the confidence interval for age calculation, but are still within error of the $^{40}Ar/^{39}Ar$ eruption age date.

The magmatic ages modeled are consistent with the $^{40}Ar/^{39}Ar$ in sanidine eruption ages and stratigraphic relationships, which geologically supports our estimate of possible minimum magmatic crystallization times (Table 3; Figs. 12 & 13) and indicates that the magmatic age results are reasonable in the geologic context. The combination of previous work in the MDVF (eruption ages, stratigraphic relationships, geophysical data showing the local crustal structure and likely depth of the pluton related to MDVF volcanism) with new U-Pb geochronologic analysis allows for a more comprehensive picture of the influences on the MDVF magmatic system. With the exception of the Whitewater Creek member of the Cooney Formation, the age model durations range from 0.04 Ma to 1.5 Ma. The Whitewater Creek member has a longer, 2.2 Ma model age range, which suggests a more protracted crystallization period.

Spatiotemporal Development of the MDVF Magmatic System

Magmatic Groups Define Pulses of Magmatism within the MDVF Flare-Up.

Based on comparison of eruption peak dates and magmatic U-Pb zircon ages (Fig. 13),

the age spectra of the ignimbrite units align with volcanic pulses defined by McIntosh, et al. (1992). Locally, the western MDVF ignimbrites reflect a different eruption tempo than the field as a whole in that there was a period of volcanic quiescence from 32.1 Ma to 31.4 Ma (McIntosh, et al., 1992). We propose two magmatic groups for the western MDVF ignimbrites examined here based on crystallization ages and magmatic evolution rather than eruption ages. The two magmatic groups are defined as 32-37.2 Ma, and 27-30 Ma.

Magmatic group 1 (32-37.2 Ma). The Bell Top 4 tuff and the Cooney Formation are designated as southern eruptive Pulse 1 by McIntosh, et al. (1992), with a timeframe of 36.2 to 33.5 Ma. Our data show overlapping age distributions indicating that zircon crystallization occurred within these magmatic systems from 37.2 ±1 Ma until 31.6±3 Ma (the youngest age concordant zircon result). The tuffs in this group are roughly contemporaneous to the Organ Caldera magmatism and the eastern MDVF – Sierra Cuchillo volcanic sequences (Fig.14). The Bell Top tuff age spectra shows one dominant peak at 34.5 Ma (Fig. 13). For the Cooney Formation units, the Whitewater Creek tuff age spectra show one dominant peak at 36.2 Ma, and a smaller peak at 34.5 Ma; the Cooney Canyon tuff spectra show only one dominant peak at 34.8 Ma. The multiple peaks the Whitewater Creek ages indicate two separate populations of zircon, which are interpreted as two periods of zircon growth in the magma chamber.

Magmatic group 2 (27-30 Ma). The Davis Canyon-age and Shelley Peak tuffs are designated as southern eruptive pulse 3A & 3B (respectively) by McIntosh, et al. (1992), with a timeframe of 29.0 to 27.4 Ma. Our data show overlapping age distributions that indicate zircon crystallization occurred within these magmatic systems from 30.7 ±2 Ma

until 27.2±2 Ma. The tuffs in this group are roughly contemporaneous to the emplacement of the Willow Springs Dome in the eastern MDVF (Fig. 13) indicating regional magmatic activity, as opposed to an isolated magmatic system.

Integrating Magmatic and Eruptive Histories: Episodic Development of the MDVF Magmatic System. Correlations between the two pulses of magmatism and eruptive stages are revealed by pulses in zircon crystallization with distinct breaks between magmatic pulses in the eastern MDVF (Figs. 12 and 13). Both eruptive stages have overlapping zircon ages, and dominant peaks in the younger pulses are preceded by distinct peaks in zircon crystallization that are interpreted to reflect separate events of magma accumulation in the upper crust. The U-Pb age dates suggest that the magmatic accumulation events began 0.4 Ma to 2.2 Ma prior to the eruptions, with possibly continuous presence of zircon saturated magma until each eruption. The episodic periodicity of magmatic events is analogous to other, large-scale, ignimbrite flare-ups (Lipman, 2007; Kern et al., 2016). The units discussed here capture the initiation and cresting of local ignimbrite output.

Zircon Insights into Magmatic Processes and Magma Dynamics

The preservation of melt compositions within zircon can be used to inform crystallization models (e.g., Zimmerer and McIntosh, 2013; Deering et al., 2016; Kern et al., 2016; Kaiser et al., 2017). The REE compositions of zircon from the eastern MDVF trace mineral fractionation within the magmatic system. During titanite crystallization, middle REEs are preferentially incorporated over Y, so Y/Dy variations may record

additional titanite fractionation in rhyolite (Fig. 5; Deering et al., 2016). The two distinct populations in sample 180-SP-1 (Fig. 5b) show a change in magma composition between core and rim to a more evolved magma during zircon residence of only 1.5 Ma.

The data show two trends in mineral fractionation in the eastern MDVF units, one dominated by amphibole/pyroxene and the second dominated by apatite/titanite. The inverse linear relationship between the calculated Ti-in-zircon temperatures and Hf content allows Hf to be utilized as a proxy for melt temperature (Fig. 8; Claiborne et al., 2006; Deering et al., 2016).

The Shelley Peak and the Davis Canyon tuffs are both attributed to the Gila Cliff Dwellings caldera source. Though petrologically similar to the Davis Canyon tuff, and of the same age (28.7 ±0.5 Ma), the difference in HREE trends between the Shelley Peak tuff and sample 78-1 indicate that these samples must come from different magmatic sources. If the Shelley Peak tuff was derived from the same magma as the Davis Canyon-age sample, the Shelley Peak zircon cores would be more depleted in mid-REEs due to magma fractionation. Therefore, sample 78-1 must not be Davis Canyon, but some other unnamed tuffaceous unit.

Zircon-Based Perspective for MDVF Magmatism

Over the course of the MDVF ignimbrite flare-up, evidence closed system magma processes are shown by the variation of compositions in the zircons sampled from those volcanic units. If the magmatic source for the Mogollon Caldera is the same system of chambers that fed the subsequent Gila Cliff Dwellings Caldera, the REE profiles should reflect the evolution and continued enrichment of melt with the passage of time. This is

shown by the enrichment of Eu from sample CC-02 (U-Pb age of 36.2 ±0.4 Ma) to MO-09 (U-Pb age of 34.8 ±0.8 Ma), and then to sample 180-SP-1 (U-Pb age of 29.6 ±0.5 Ma).

CONCLUSIONS

U-Pb ages of zircon in magmas during the 36-24 Ma MDVF ignimbrite flare-up were determined by SHRIMP-RG. These data reveal age spectra with dominant peaks of autocrysts. Xenocrysts are rare to absent. Modeled magmatic ages are consistent with observed eruptive stratigraphic relationships. The U-Pb in zircon ages record epsiodicity in the magmatic history of the MDVF. These ages fall into two groups defining distinct pulses of magmatism that correlate with eruptive pulses, but indicate that magmatic construction began 40,000 to 2.2 million years prior to eruption. The model magmatic ages (Table 3) represent the minimum pre-eruptive magmatic residency of reservoir magmas in the MDVF. These durations indicate that thermochemical conditions for zircon saturation were maintained for extended periods. Although xenocrysts are present, they are rare, suggesting limited inheritance.

The episodicity revealed by the zircon U-Pb ages of the western MDVF flare-up can be interpreted in the context of continental arc magmatic systems in general. The first pulse marks the regional initiation of the flare-up, as the crystal poor top of the rhyolitic chamber is emptied and the caldera subsequently collapses. The second regional pulse brings more crystal-rich evolved mush to the surface from a different eruptive center.

REFERENCES CITED

Annen, C., Blundy, J.D., and Sparks, R.S.J., 2006, The genesis of intermediate and silicic magmas in deep crustal hot zones: Journal of Petrology, v. 47, no. 3, p. 505-539, doi: 10.1093/petrology/egi084.

Bachmann, O.B., and Bergantz, G.W., 2008, Deciphering magma chamber dynamics from styles of compositional zoning in large silicic ash flow sheets: Reviews in Mineralogy & Geochemistry, v. 69, p. 651-674.

Best, M.G., and Christiansen, E.H., 1991, Limited extension during peak Tertiary volcanism, Great Basin of Nevada and Utah: Journal of Geophysical Research: Solid Earth, v. 96, no. B8, p. 13509-13528.

Bickerman, M., Bell, K., Card, J.W., 1992, Strontium and neodymium isotopic study of the western Mogollon-Datil volcanic region, New Mexico, U.S.A.: Contributions to Mineralogy and Petrology, v. 109 (4), p. 459-470.

Bickerman, M., 1989, Rb, Sr, Rb-Sr, and isotopic Sr values for volcanic rocks from the southwestern part of the Mogollon-Datil volcanic field: New Mexico Geology, p. 76-82.

Bickerman, M., 1994, Are the western Mogollon-Datil mid-Cenozoic ash flows cogenetic? Pearce element ration and isotopic aspects of the question: New Mexico Geological Society Guidebook, 45th Field Conference, Mogollon Slope, West-Central New Mexico and East-Central Arizona, p. 187- 192.

Bowring, S.A., Karlstrom, K.E., 1990, Growth, stabilization, and reactivation of Proterozoic lithosphere in the southwestern United States: Geology, v. 18, p. 1203-1206.

Bucholz, C.E., Eddy, M.P., Jagoutz, O., Bowring, S.A., Schmidt, M.W., and Sambuu, O., 2017, Constraining the time scales of magmatic differentiation with U-Pb zircon geochronology: Geology, v. 45, no. 1, p. 11-14, doi: 10.1130/G38505.1.

Caricchi, L., Simpson, G., and Schaltegger, U., 2016, Estimates of volume and magma input in crustal magmatic systems from zircon geochronology: The effect of modeling assumptions and system variables: Frontiers in Earth Science, v. 4, no. 48, 16p.

Carley, T.L., Miller, C.F., Wooden, J.L., Padilla, A.J., Schmitt, A.K., Economos, R.C., Bindeman, I.N., and Jordan, B.T., 2014, Iceland is not a magmatic analog for the Hadean: Evidence from the zircon record: Earth and Planetary Science Letters, v. 405, p. 85-97.

Cather, S.M., 1990, Stress and volcanism in the northern Mogollon-Datil volcanic field, New Mexico: Effects of the post-Laramide tectonic transition: Geological Society of America Bulletin, v. 102, p. 1447-1458.

Chapin, C.E., McIntosh, W.C., and Chamberlin, R.M., 2004, The late Eocene-Oligocene peak of Cenozoic volcanism in southwestern New Mexico, *in* Mack, G.H, and Giles, K.A., eds., The Geology of New Mexico, A Geologic History: New Mexico Geological Society, Special Publication 11, p. 271-293.

Claiborne, L.L., Miller, C.F., Walker, B.A., Wooden, J.L., Mazdab, F.K., and Bea, F., 2006, Tracking magmatic processes through Zr/Hf ratios in rocks and Hf and Ti zoning in zircons: An example from the Spirit Mountain batholith, Nevada: Mineralogical Magazine, v.70, p. 517-543, doi: 10.1180/0026461067050348.

Clemons, R.E., 1975, Petrology of the Bell Top Formation, *in* Seager, W.R., Clemons, R.E., and Callender, J.F., eds., Las Cruces Country, New Mexico Geological Society 26th Annual Fall Field Conference Guidebook, p. 123-130.

Corfu, F., Hanchar, J.M., Hoskin, P.W.O., and Kinny, P., 2003, Atlas of zircon textures, in Hanchar J.M., and Hoskin P.W.O., eds., Mineralogical Society of America, Reviews in Mineralogy and Geochemistry, v. 53, p. 468-500.

Davis, J.M., and Hawkesworth, C.J., 1994, Early calk-alkaline magmatism in the Mogollon-Datil Volcanic Field, New Mexico, USA: Journal of the Geological Society, London, v. 151, p.825-843.

Davis, J.M., and Hawkesworth, C.J., 1995, Geochemical and tectonic transitions in the evolution of the Mogollon-Datil volcanic field, New Mexico, U.S.A.: Chemical Geology, v. 119, p. 31-53.

Deering, C.D., Keller, B., Schoene, B., Bachmann, O., Beane, R., and Ovtcharova, M., 2016, Zircon record of the plutonic-volcanic connection and protracted rhyolite melt evolution: Geology, v. 44, no. 4, p. 267-270, doi: 10.1130/G37539.1.

de Silva, S.L., and Gosnold, W.D., 2007, Episodic construction of batholiths: Insights from the spatiotemporal development of an ignimbrite flare-up: Journal of Volcanology and Geothermal Research, v. 167, no. 1-4, p. 320-335.

Elston, W.E., Coney, P., and Rhodes, R.C., 1970, Progress report on the Mogollon Plateau Volcanic Province, southwestern New Mexico: No. 2*, *in* Woodward, L.A., ed., Tyrone-Big Hatchet Mountain-Florida Mountains Region: New Mexico Geological Society, 21st Annual Field Conference, Guidebook, p. 75-86.

Elston, W.E., 2008, When batholiths exploded: The Mogollon-Datil volcanic field, southwestern New Mexico, *in* Mack, G., Witcher, J., and Lueth, V.W., eds., Geology of the Gila area wilderness- Silver City area: New Mexico Geological Society Guidebook, 59th Field Conference, p. 117-128.

Farmer, L.G., Bailley, T., Elkins-Tanton, L.T., 2007, Mantle source volumes and the origin of the mid-tertiary ignimbrite flare-up in the southern Rocky Mountains, western U.S.: Lithos, v. 102, p. 279-294.

Ferry, J.M., and Watson, E.B., 2007, New thermodynamic models and revised calibrations for the Ti-in-zircon and Zr-in-rutile thermometers: Contributions to Mineralogy and Petrology, v. 154, p. 429-437, doi 10.1007/s00410-007-0201-0.

Finch, R.J., and Hanchar, J.M., 2003, Structure and chemistry of zircon and zircon-group minerals, *in* Hanchar, J.M., and Hoskin, P.W.O., eds., Mineralogical Society of America, Reviews in Mineralogy and Geochemistry, v. 53, p. 1-25.

Finnell, T.L., and Ratté, J.C., 2006, Preliminary Geologic map of the Luna quadrangle, Catron County, New Mexico: New Mexico Bureau of Geology and Mineral Resources Open-file Map Series OFGM 129, scale 1:24000, 1 sheet.

Foster, D.A., Mueller, P.A., Heatherington, A., Gifford, J.N., and Kalakay, T.J., 2012, Lu-Hf systematics of magmatic zircons reveal a Proterozoic crustal boundary under the Cretaceous Pioneer batholith, Montana: Lithos, v. 142-143, p. 216-225.

Gaschnig, R.M., Vervoort, J.D., Lewis, R.S., and McClelland, W.C., 2010, Migrating magmatism in the northern US Cordillera: in situ U-Pb geochronology of the Idaho batholith: Contributions to Mineralogy and Petrology, v. 159, p. 863-883, doi: 10.1007/s00410- 009-0459-5.

Gans, P.B., and Bohrson, W.A., 1998, Suppression of volcanism during rapid extension in the Basin and Range Province, United States: Science, v. 279, no. 5347, p. 66-68.

Glazner, A., Bartley, J.M., Coleman, D.S., Gray, W., and Taylor, R.Z., 2004, Are plutons assembled over millions of years by amalgamation from small magma chambers?: GSA Today, v. 14, no. 4/5, p. 4-11.

Glazner, A.F., and Ussler, W., 1989, Crustal extension, crustal density, and the evolution of Cenozoic Magmatism in the Basin and Range of the western United States: Journal of Geophysical Research-Solid Earth and Planets, v. 94, no. B6, p. 7952-7960.

Grimes, C.B., Wooden, J.L., Cheadle, M.J., and John, B.E., 2015, "Fingerprinting" tectono-magmatic provenance using trace elements in igneous zircon: Contributions to Mineralogy and Petrology, v. 170, no. 46, 26 p., doi: 10.1007/s00410-015-1199-3.

Hanchar, J.M., and Watson, E.B., 2003, Zircon saturation thermometry in Hanchar, J.M., and Hoskin, P.W.O., eds., Mineralogical Society of America, Reviews in Mineralogy and Geochemistry, v. 53, p. 89-110.

Hanchar, J.M., and van Westrenen, W., 2007, Rare earth element behavior in zircon-melt systems: Elements, v. 3, p. 37-42.

Harley, S.L., and Kelly, N.M., 2007, Zircon, Tiny but timely: Elements, v. 3, no. 1, p. 13-18.

Hildreth, W., and Moorbath, S., 1988, Crustal contributions to arc magmatism in the Andes of Central Chile: Contributions to Mineralogy and Petrology, v. 98, p. 455-489.

Hoskin, P.W.O., and Schaltegger, U., 2003, The composition of zircon and igneous and metamorphic petrogenesis, *in* Hanchar, J.M., and Hoskin, P.W.O., eds., Mineralogical Society of America, Reviews in Mineralogy and Geochemistry, v. 53, p. 27-62.

Kaiser, J.F., de Silva, S., Schmitt, A.K., Economos, R., and Sunagua, M., 2017, Million-year melt-presence in monotonous intermediate magma for a volcanic-plutonic assemblage in the Central Andes: Contrasting histories of crystal-rich and crystal-poor super-sized silicic magmas: Earth and Planetary Science Letters, v. 457, p. 73-86.

Kern, J.M., de Silva, S., Schmitt, A.K., Kaiser, J.F., Iriarte, A.R., and Economos, R., 2016, Geochronological imaging of an episodically constructed subvolcanic batholith: U-Pb in zircon chronochemistry of the Altiplano-Puna Volcanic Complex of the Central Andes: Geosphere, v. 12, no. 4, p. 1-24, doi: 10.1130/GES01258.1.

Kirkland, C.L., Smithies, R.H., Taylor, R.J.M., Evans, N., and McDonald, B., 2014, Zircon Th/U ratios in magmatic environs: Lithos, v. 212-215, p. 397-414, doi: 10.1016/j.lithos.2014.11.021.

Lipman, P.W., 2007, Incremental assembly and prolonged consolidation of Cordilleran magma chambers: evidence from the Southern Rocky Mountain volcanic field: Geosphere, v. 3, no. 1, p. 42-70.

Ludwig, K., 2008, A geochronological toolkit for Microsoft Excel: Berkeley Geochronology Center. Special Publication, no. 4, p. 77.

Ludwig, K., 2009, SQUID 2: A user's manual: Berkeley Geochronology Center Special Publication, rev. 12 April, 2009, v. 5, p. 110.

Mack, G.H., Nightengale, A.L., Seager, W.R., and Clemons R.E., 1994, The Oligocene Goodsight-Cedar Hills half graben near Las Cruces and its implications to the

evolution of the Mogollon-Datil volcanic field and to the southern Rio Grande rift *in* Chamberlin, R.M., Kues, B.S., Cather, S.M., Barker, J.M., McIntosh, W.C., eds., Mogollon Slope (West-Central New Mexico and East-Central Arizona): New Mexico Geological Society 45th Annual Fall Field Conference Guidebook, 335p.

Mahood, G., and Hildreth, W., 1983, Large partition coefficients for trace elements in high-silica rhyolites: Geochimica et Cosmochimica Acta, v. 47, p. 2155-2170.

McDougall, I., and Harrison, T.M., 1999, Geochronology and Thermochronology by the $^{40}Ar/^{39}Ar$ Method: Oxford University Press On Demand, 288p.

McDowell, S.M., Miller, C.F., Mundil, R., Ferguson, C.A., and Wooden, J.L., 2014, Zircon evidence for a ~200 k.y. supereruption-related thermal flare-up in the Miocene southern Black Mountains, western Arizona, USA: Contributions to Mineralogy and Petrology, v. 167, no. 1031, p. 1-21, doi: 10.1007/s00410-014-1031-5.

McIntosh, W.C., Chapin, C.E., Ratté, J.C., and Sutter J.F., 1992, Time-stratigraphic framework for the Eocene-Oligocene Mogollon-Datil volcanic field, southwest New Mexico: Geological Society of America Bulletin, v. 104, no. 7, p. 851-871.

McMillan, N.J., 1998, Temporal and spatial magmatic evolution of the Rio Grande rift *in* Mack, G.H., Austin, G.S., and Barker, J.M., eds., Las Cruces Country II: New Mexico Geological Society 49th Annual Fall Field Conference Guidebook, p. 107-116.

McMillan, N.J., 2004, Magmatic record of Laramide subduction and the transition to Tertiary extension: Upper Cretaceous through Eocene igneous rocks of New Mexico *in* Mack, G.H, and Giles, K.A., eds., The Geology of New Mexico, A Geologic History: New Mexico Geological Society, Special Publication 11, p. 249-270.

McMillan, N.J., Dickin, A.P., and Haag, D., 2000, Evolution of magma source regions in the Rio Grande rift, southern New Mexico: Geological Society of the Americas Bulletin, v. 112, no. 10, p. 1582-1593.

Menard, H.W., 1978, Fragmentation of the Farallon Plate by pivoting subduction: The Journal of Geology, v. 86, no. 1, p. 99-110.

Michelfelder, G.S., and McMillan, N.J., 2012, Geochemistry, origin, and U-Pb zircon ages of the Sierra Cuchillo laccolith, Sierra County, New Mexico: New Mexico Geological Society Guidebook, 63rd Field Conference, Sierra County, p. 121-132.

Miller, C.F., McDowell, S.M., and Mapes, R.W., 2003, Hot and cold granites? Implications of zircon saturation temperatures and preservation of inheritance: Geology, v. 31, no. 6, p. 529-532.

Miller, J.S., and Wooden, J.L., 2004, Residence, resorption and recycling of zircons in Devils Kitchen Rhyolite, Coso Volcanic Field, California: Journal of Petrology, v. 45, no. 11, p. 2155-2170, doi: 10.1093/petrology/egh051.

Ramos, F.C., Heizler, M.T., Buettner, J.E., Gill, J.B., Wei, H.Q., Dimond, C.A., and Scott, S.R., 2016, U-series and $^{40}Ar/^{39}Ar$ ages of Holocene volcanic rocks at Changbaishan volcano, China: Geology, v. 44, no. 7, p. 511-514, doi: 10.1130/G37837.1.

Ratté, J.C., 1981, Geologic map of the Mogollon quadrangle, Catron County, New Mexico: U.S. Geological Survey Map and Chart Series GQ-1557, scale 1:24,000, 1 sheet.

Ratté, J.C., Marvin, R.F., and Naeser, C.W., 1984, Calderas and ash flow tuffs of the Mogollon Mountains, southwestern New Mexico: Journal of Geophysical Research, v. 89, no. B10, p. 8713-8732.

Ratté, J., Lynch, S., and McIntosh, B., 2006, Draft Geologic map of the Holt Mountain quadrangle, Catron County, New Mexico: New Mexico Bureau of Geology and Mineral Resources Open-file Map Series OFGM 120, scale unknown, 1 sheet.

Rosenblum, S., 1958, Magnetic Susceptibilities of minerals in the Frantz isodynamic magnetic separator: The American Mineralogist, v. 43, p. 170-173.

Salings, E., 2017, Magma Evolution in the Bursum Ignimbrite Complex, western Mogollon-Datil Volcanic Field, New Mexico: Evidence for Zoning of a Rhyolite

Magma by Remobilization of a Crystal Mush [Master's thesis]: Missouri State University, 147 p.

Schneider, R.V., and Keller, G.R., 1994, Crustal structure of the western margin of the Rio Grande rift and Mogollon-Datil volcanic field, southwestern New Mexico and southeastern Arizona *in* Keller G.R., and Cather S.M., eds., Basins of the Rio Grande Rift: Structure, Stratigraphy, and Tectonic Setting: Boulder, Colorado, Geological Society of America Special Paper 291, p. 207-226.

Seager, W.R., 1975, Cenozoic Tectonic Evolution of the Las Cruces area, New Mexico *in* Seager, W.R., Clemons, R.E., Callender, J.F., eds., Las Cruces Country: New Mexico Geological Society 26th Annual Fall Field Conference Guidebook, 376 p.

Seager, W., 2004, Laramide (Late-Cretaceous-Eocene) tectonics of southwestern New Mexico *in* Mack, G.H, and Giles, K.A., eds., The Geology of New Mexico, A Geologic History: New Mexico Geological Society, Special Publication 11, p. 183-202.

Sircombe, K.N., and Stern, R.A., 2002, An investigation of artificial biasing in detrital zircon U-Pb geochronology due to magnetic separation in sample preparation: Geochimica et Cosmochimica Acta, v. 66, no. 13, p. 2379-2397.

Smith, M.P., Storey, C.D., Jeffries, T.E., and Ryan, C., 2009, In situ U-Pb and trace element analysis of accessory minerals in the Kiruna District, Norrbotten, Sweden: New constraints on the timing and origin of mineralization: Petrology, v. 50, no. 11, p. 2063- 2094, doi:10.1093/petrology/egp069.

Strauss, J.V., Hoiland, C.W., Ward, W., Johnson, B.G., Nelson, L.L., and McClelland, W.C., 2016, Orogen transplant: Taconic-Caledonian arc magmatism in the central Brooks Range of Alaska: GSA Bulletin, doi:10.1130/B31593.1.

Thompson, R.N., Ottley, C.J., Smith, P.M., Pearson, D.G., Dickin, A.P., Morrison, M.A., Leat, P.T., and Gibson, S.A., 2005, Source of the Quaternary alkali basalts, picrites and basanites of the Potrillo Volcanic Field, New Mexico, USA: Lithosphere or convecting mantle?: Journal of Petrology, v. 46, no. 8, p. 1603-1643, doi: 10.1093/petrology/egi028.

Wasson, J.T., 1985, Meteorites: their record of early solar-system history: W.H. Freeman and Co., New York, NY.

Watson, E.B., and Harrison, T.M., 1983, Zircon saturation revisited: temperature and compositional effects in a variety of crustal magma types: Earth and Planetary Science Letters, v. 64, p. 295-304.

Watson, E.B., and Harrison, T.M., 2005, Zircon thermometer reveals minimum melting conditions on earliest Earth: Science, v. 308, p. 841-844.

Wilson, C.J.N., and Charlier, B.L.A., 2016, The life and times of silicic volcanic systems: Elements, v. 12, p. 103-108, doi: 10.2113/gsaelements.12.2.103.

Wotzlaw, J., Schaltegger, U., Frick, D.A., Dungan, M.A., Gerdes, A., and Günther, D., 2013, Tracking the assembly of large-volume silicic magma reservoirs from assembly to supereruption: Geology, v. 41, p. 867-870, doi: 10.1130/G34366.

Zimmerer, M.J., and McIntosh, W.C., 2013, Geochronologic evidence of upper-crustal in situ differentiation: Silicic magmatism at the Organ complex, New Mexico: Geosphere, v. 9, no. 1, p. 155-169, doi: 10.1130/GES00841.1.

Table 1. Summary of units, their sources, eruption ages, and approximate volumes.

Tuff	Source Caldera	Eruption age[1] (Ma) ($1\sigma \pm 5\%$)	Estimated[2] erupted volume in km^3
Cooney Formation	Mogollon	~ 34	>100
Whitewater Creek member Cooney Canyon member South Fork member			
Bell Top tuff 4	Organ (?)	34.96	
Davis Canyon tuff	Gila Cliff Dwellings	29.01	200-400
Shelley Peak tuff	Gila Cliff Dwellings	28.1	100-200

[1]Eruption ages are from $^{40}Ar/^{39}Ar$ in sanidine from McIntosh et al., 1992 except for the Cooney Fm. estimation which is an average from K-Ar in biotite

[2]Cooney eruption volume is from Ratté et al., 1984. All other eruption volumes are from McIntosh et al., 1992.

Table 2. Zircon trace elements results.

Spot Name	Fe (ppm)	Y (ppm)	La (ppm)	Ce (ppm)	Nd (ppm)	Sm (ppm)	Eu (ppm)	Gd (ppm)	Dy (ppm)	Er (ppm)	Yb (ppm)	Hf (ppm)	Eu (star)
180-SP-1-1.1	0.18	2198	0.0296	74	3.6	7.2	3.2	56	219	384	655	7933	0.48
180-SP-1-1.2	0.32	672	0.0078	55	0.2	0.9	0.3	8	42	126	345	12598	0.37
180-SP-1-2.1	0.11	251	0.0059	25	0.1	0.2	0.1	2	12	48	167	14144	0.36
180-SP-1-6.1	0.95	3850	0.1393	140	7.0	14.1	5.3	105	394	651	1070	9716	0.42
180-SP-1-4.1	0.17	1209	0.0233	33	2.6	5.6	2.5	37	127	202	338	7914	0.53
180-SP-1-5.1	0.33	1845	0.0239	107	1.4	3.4	1.3	33	159	331	652	10813	0.38
180-SP-1-8.1	0.20	1649	0.0158	66	1.5	3.5	1.6	30	143	298	571	8592	0.49
180-SP-1-4.2	0.49	835	0.0068	74	0.3	0.7	0.3	8	49	153	476	13894	0.36
180-SP-1-7.2	0.57	1331	0.0176	52	1.3	3.4	1.2	28	128	249	458	10694	0.39
180-SP-1-7.1	0.18	1306	0.0131	113	0.5	1.4	0.5	13	78	236	669	12311	0.37
180-SP-1-3.1	1.82	1402	0.0521	50	3.3	6.4	2.8	44	149	234	389	8369	0.51
UV-R2-8.1	0.20	1175	0.0096	30	0.9	3.0	1.3	28	111	215	396	10714	0.43
UV-R2-2.1	0.13	1124	0.0131	38	0.8	2.1	0.9	23	97	195	382	9459	0.39
UV-R2-4.1	0.19	2531	0.0277	83	3.3	7.4	2.3	64	253	448	762	10898	0.32

Spot Name	Fe (ppm)	Y (ppm)	La (ppm)	Ce (ppm)	Nd (ppm)	Sm (ppm)	Eu (ppm)	Gd (ppm)	Dy (ppm)	Er (ppm)	Yb (ppm)	Hf (ppm)	Eu (star)
UV-R2-5.1	0.16	1192	0.0113	59	0.6	2.3	0.7	22	107	220	423	11597	0.33
UV-R2-3.1	0.26	621	0.0074	34	0.2	0.8	0.3	8	49	119	275	12820	0.32
UV-R2-6.2	25.89	1713	4.1059	224	8.0	6.8	1.3	42	166	297	521	10891	0.24
UV-R2-1.1	0.90	1093	0.2476	52	1.9	3.1	1.1	25	99	191	357	9326	0.39
UV-R2-6.1	0.14	1072	0.0110	50	0.3	1.3	0.4	14	88	202	435	12379	0.26
UV-R2-7.1	4.27	1989	0.0378	27	4.1	8.3	3.4	54	201	350	622	9362	0.48
78-1-1.1	1.57	1906	0.0722	46	4.1	9.3	4.4	61	203	332	576	7609	0.56
78-1-3.1	0.87	1057	0.0119	24	0.9	2.6	1.5	22	95	192	380	7987	0.60
78-1-12.1	0.83	1826	0.0093	49	1.5	4.4	2.4	37	166	333	629	9152	0.56
78-1-6.1	0.43	1304	0.0120	30	2.1	5.6	3.0	41	138	227	401	9273	0.60
78-1-2.1	1.04	1242	0.0101	27	0.8	2.8	1.4	26	108	224	456	9272	0.50
78-1-4.1	49.14	2066	0.0835	48	4.4	9.0	5.0	63	221	384	697	8074	0.63
78-1-10.2	1.58	1732	0.0428	41	3.4	6.8	3.5	47	178	315	563	9278	0.60
78-1-10.1	0.50	1931	0.0247	45	3.8	7.4	4.0	57	198	335	609	9672	0.59
78-1-8.1	0.72	3103	0.0648	61	6.7	13.0	7.3	90	316	521	914	8171	0.65
78-1-5.1	4.42	1284	0.0135	7	0.9	2.5	1.5	24	118	218	388	9218	0.61
78-1-13.1	4.66	2449	0.0219	79	2.2	5.7	3.7	57	236	423	780	8657	0.62
78-1-14.1	0.63	1772	0.0221	35	3.8	7.1	3.7	50	172	300	543	9074	0.60
78-1-7.1	0.92	1160	0.0146	25	1.0	2.7	1.6	25	106	212	426	8825	0.60

Spot Name	Fe (ppm)	Y (ppm)	La (ppm)	Ce (ppm)	Nd (ppm)	Sm (ppm)	Eu (ppm)	Gd (ppm)	Dy (ppm)	Er (ppm)	Yb (ppm)	Hf (ppm)	Eu (star)
78-1-9.1	0.78	1419	0.0101	30	1.1	3.6	1.7	29	128	248	513	10097	0.52
78-1-11.1	0.31	3157	0.1046	61	7.2	14.2	7.9	101	330	537	911	8715	0.63
78-1-15.1	0.70	1401	0.0253	28	2.3	5.2	2.6	36	129	245	444	9090	0.57
78-1-3.2	4.85	876	0.0740	23	0.8	2.1	1.2	17	80	159	323	8851	0.61
CC-02-1.1	124.00	3297	0.0170	119	3.8	9.6	1.8	75	295	568	987	9793	0.20
CC-02-2.1	29.30	2055	0.0396	86	5.3	9.1	2.8	62	197	361	615	8528	0.36
CC-02-5.1	62.13	1774	1.0199	85	3.4	6.1	2.3	44	171	303	558	12152	0.43
CC-02-7.1	0.76	1772	0.0110	68	0.7	2.4	0.6	25	138	320	660	11875	0.22
CC-02-8.1	5.38	3969	0.0272	161	4.0	9.7	1.8	77	335	687	1285	12638	0.20
CC-02-6.1	21.60	3353	0.1120	140	7.9	15.0	4.0	100	345	570	942	10186	0.32
CC-02-4.1	0.69	1448	0.0089	69	0.8	2.7	0.5	26	131	265	494	11688	0.20
CC-02-3.1	2.62	2683	0.0150	102	2.3	5.9	1.5	53	228	457	809	9898	0.27
MO-09-7.1	0.14	1742	0.0199	40	1.8	4.1	1.7	37	156	322	658	9759	0.42
MO-09-4.1	1.46	1127	0.1894	31	0.8	2.2	1.1	21	99	213	429	9184	0.50
MO-09-6.1	0.12	1843	0.0269	30	3.5	5.8	3.1	48	173	327	601	9116	0.56
MO-09-5.1	0.33	656	0.0180	50	0.6	1.5	0.5	12	56	120	256	10358	0.38

Spot Name	Fe (ppm)	Y (ppm)	La (ppm)	Ce (ppm)	Nd (ppm)	Sm (ppm)	Eu (ppm)	Gd (ppm)	Dy (ppm)	Er (ppm)	Yb (ppm)	Hf (ppm)	Eu (star)
MO-09-1.1	0.18	594	0.0143	19	0.4	1.3	0.6	12	52	109	232	9067	0.44
MO-09-3.1	0.12	475	0.0036	16	0.2	0.7	0.3	7	39	89	213	10504	0.41
MO-09-2.1	14.91	968	0.0371	16	0.7	2.3	0.1	21	93	170	304	10467	0.04

Table 3. U-Pb in zircon age date results for study units compared to $^{40}Ar/^{39}Ar$ eruption ages, with possible zircon magmatic residence times.

Tuff	U-Pb zircon Age (Ma)	n	MSWD	Eruption age[1] (Ma) (1σ ± 5%)	Estimated magma residence time (Ma)
Cooney Formation				~ 34	
Whitewater Creek	36.2 ± 0.4	7	1.25		2.2
Cooney Canyon	34.8 ± 0.8	6	0.24		0.8
Bell Top tuff 4	34.5 ± 0.5	9	0.84	34.96	0.04
Davis Canyon–age tuff	28.7 ± 0.5	12	1.00	29.01	0.19
Shelley Peak tuff	29.6 ± 0.5	10	1.09	28.1	1.5

[1]Eruption ages are from $^{40}Ar/^{39}Ar$ in sanidine from McIntosh et al. (1992) except for the Cooney Fm. estimation which is an average from K-Ar in biotite

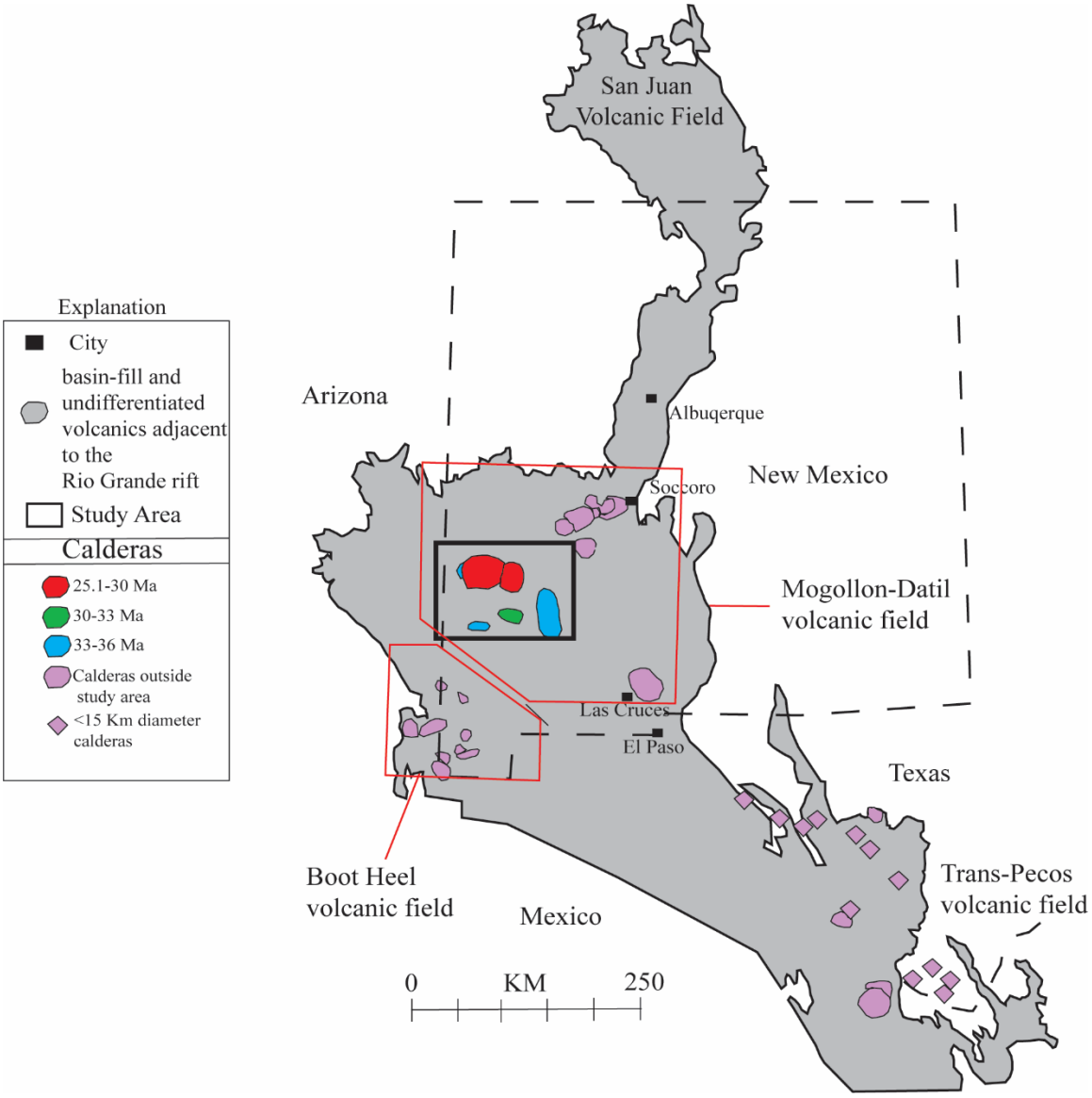

Figure 1. Generalized map showing the distribution of calderas within the Rio Grande rift and New Mexico. Modified from Michelfelder and McMillan (2012) after Chapin et al. (2004). Black rectangle shows the study area. Color designations of calderas correspond to magmatic pulse designations of McIntosh et al., 1992.

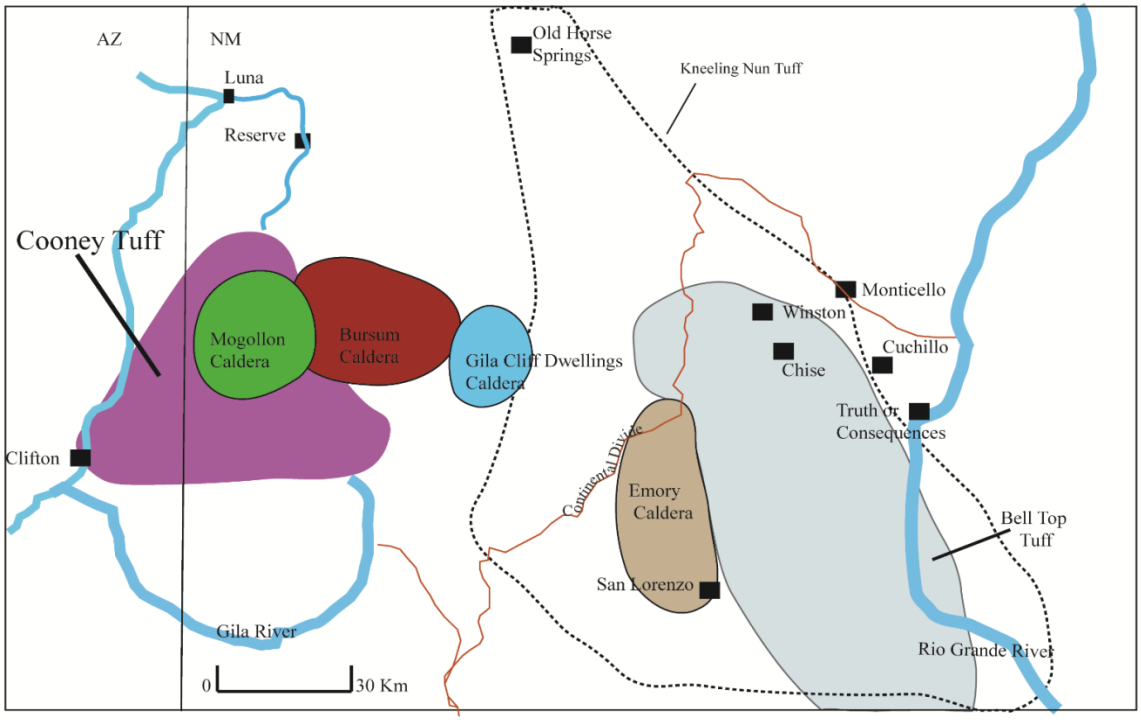

Figure 2. Regional map of the western MDVF showing the extent of the Cooney and Bell Top tuff with source calderas. Outlines from Ratté et al. (1984).

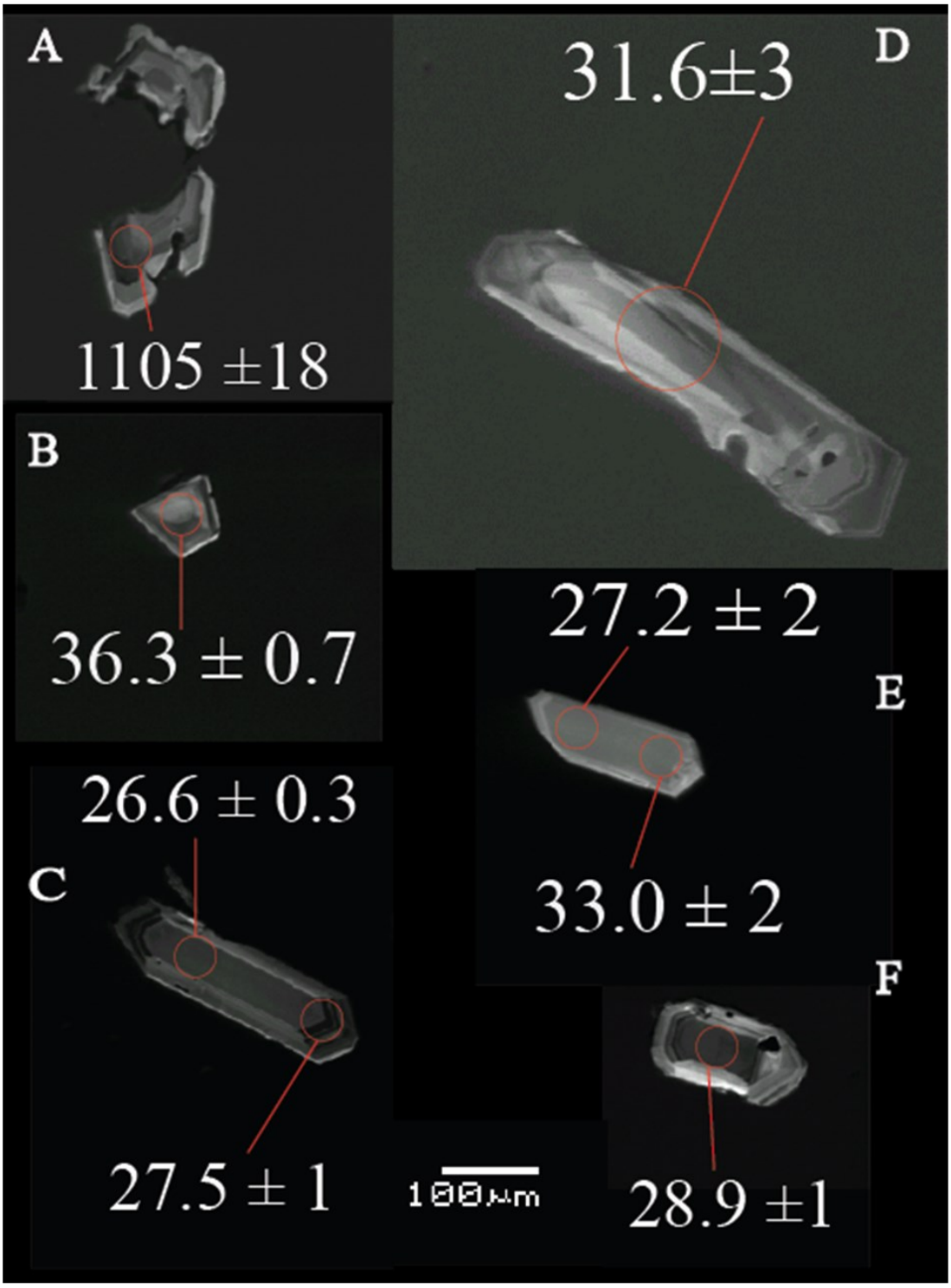

Figure 3. Cathodoluminescence images of representative zircon crystals with analysis spots and corresponding ages. A. Xenocrystic zircon from the Whitewater Creek tuff. B. Whitewater creek tuff. C. Shelley Peak tuff. D. Bell Top tuff. E. Davis Canyon "age" tuff. F. Shelley Peak tuff.

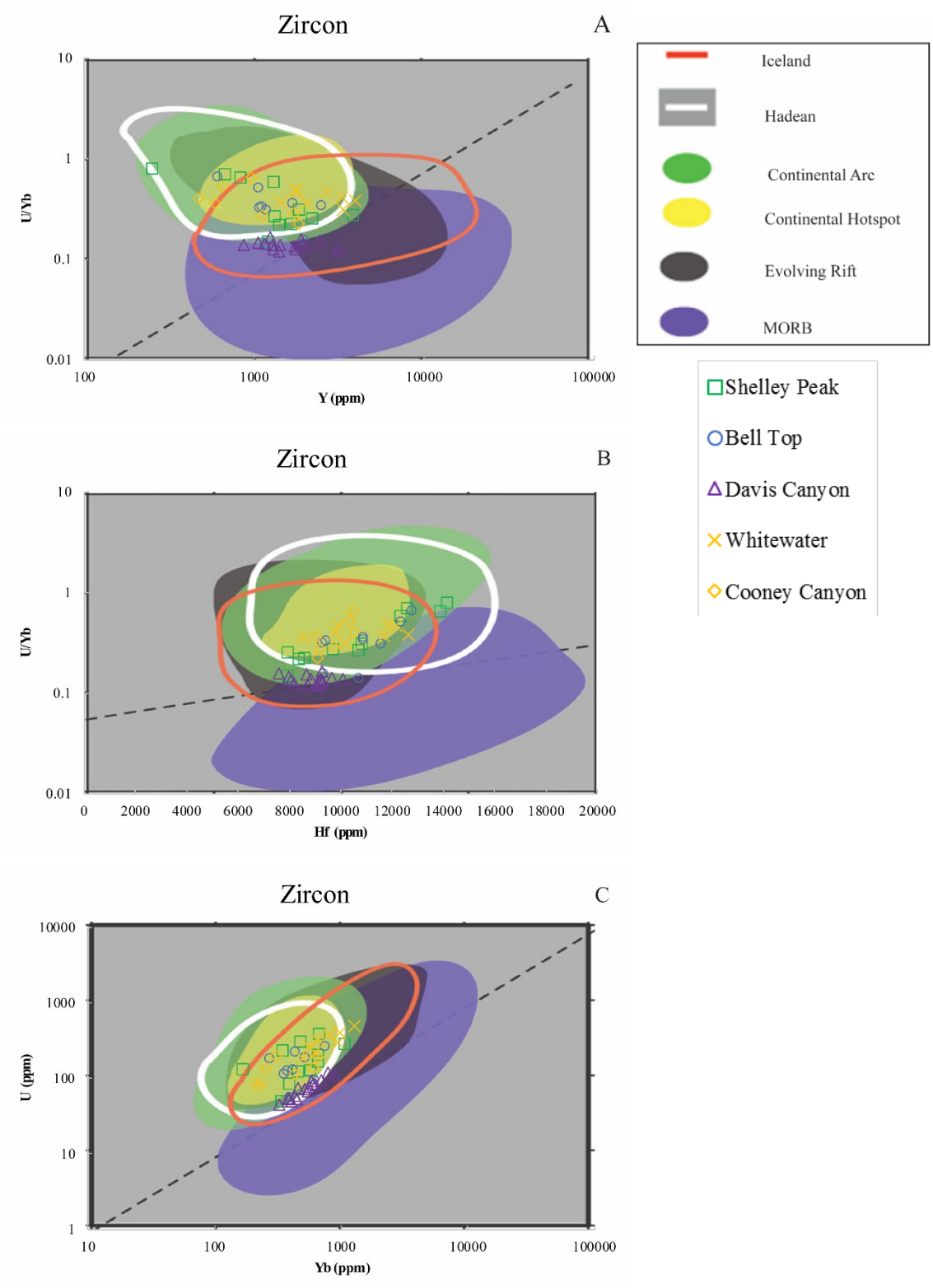

Figure 4. Trace element concentrations and ratios of the MDVF zircon samples within a global context (modified from Carley et al., 2014).

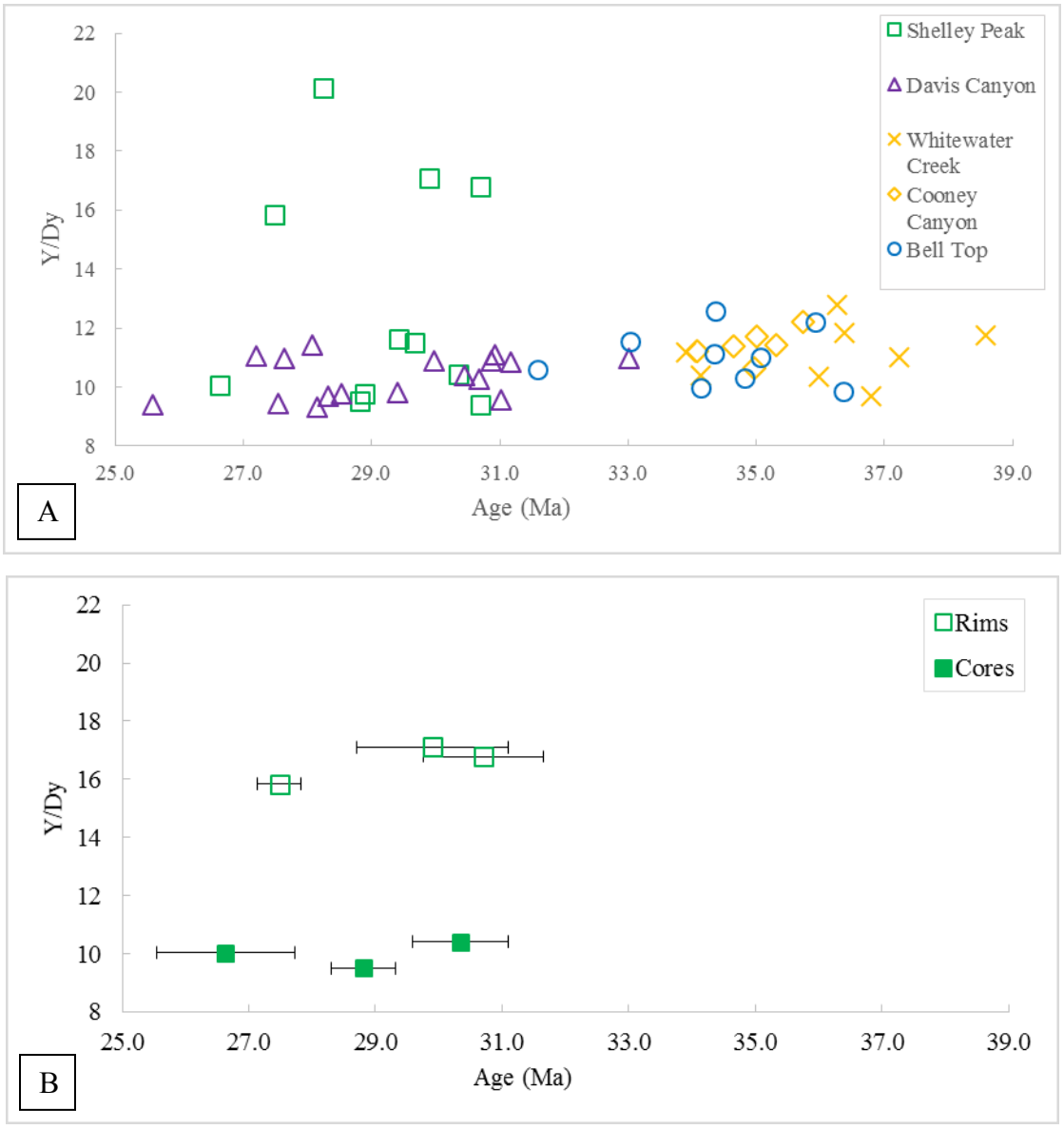

Figure 5. The time interval in which Y/Dy differs provides an estimation of the duration of melt extraction and accumulation. A) Cumulative results from MDVF analyses. B) Comparison between rim and core analyses from a single unit (180-SP-1).

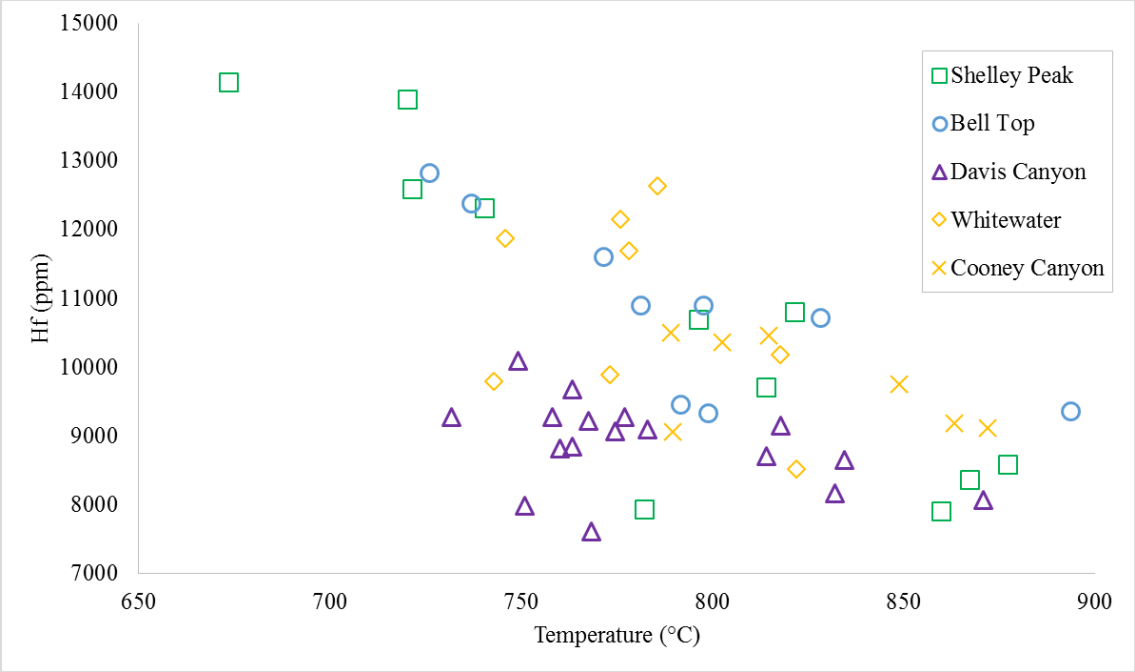

Figure 6. Hf (ppm) vs. Ti (˚C temperature) diagram for MDVF samples. Error is within symbol size

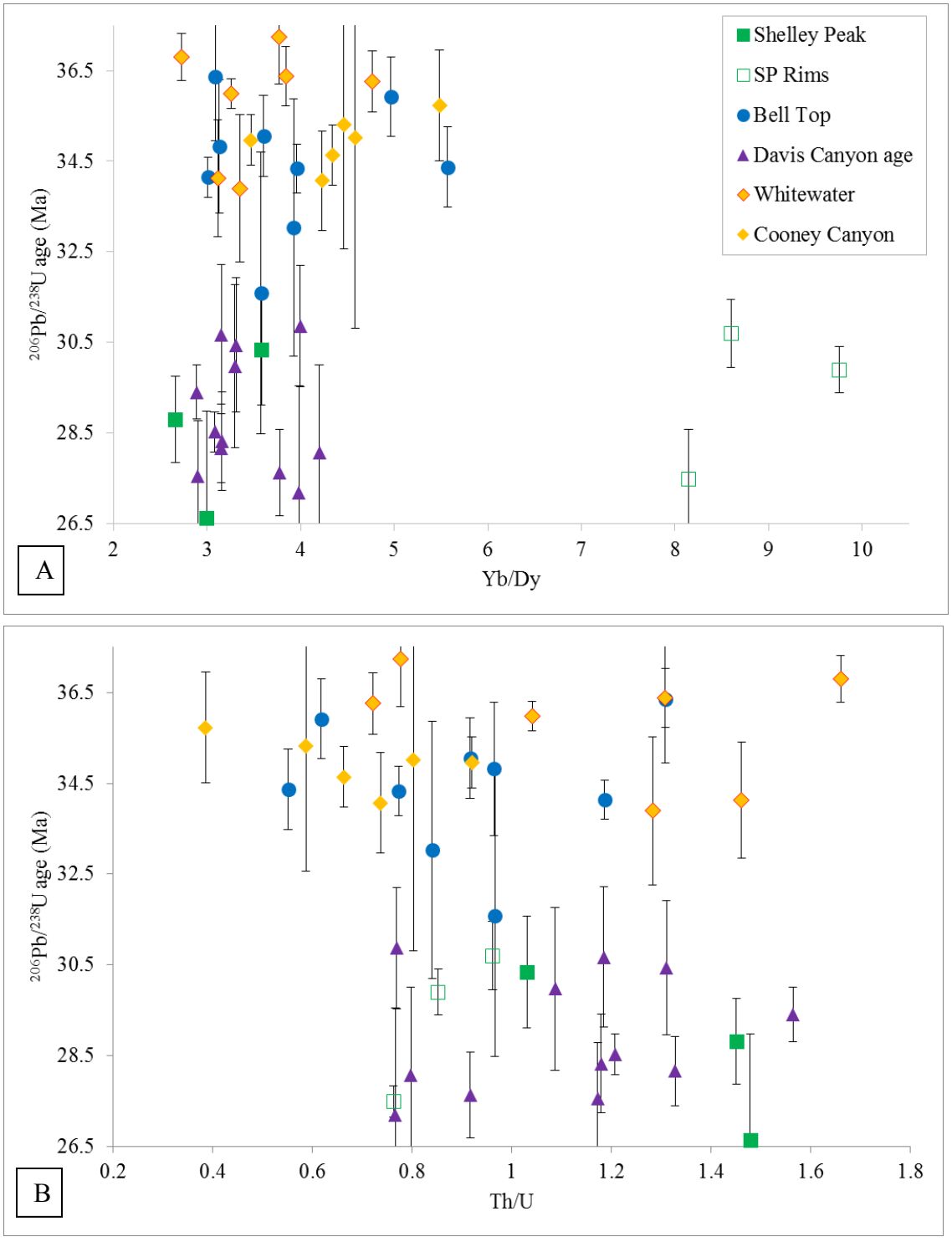

Figure 7. A. Yb/Dy vs. $^{206}Pb/^{238}U$ age (Ma) for MDVF zircon samples. Increasing Yb/Dy indicates increasing melt crystallization. B. Th/U vs. $^{206}Pb/^{238}U$ age (Ma) for MDVF zircon samples. Decreasing U/Th indicates decreasing melt temperature

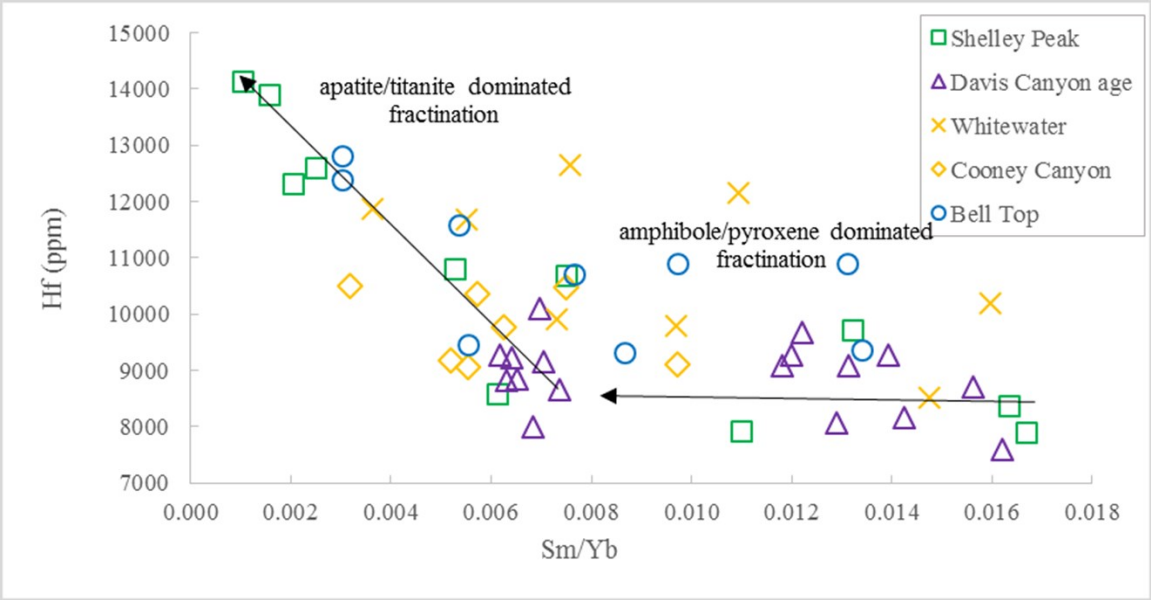

Figure 8. Hf concentration vs Sm/Yb ratio diagram for MDVF zircon analyses. Trend lines illustrate mineral fractionation trends of apatite/titanite and amphibole/pyroxene fractionation during crystallization.

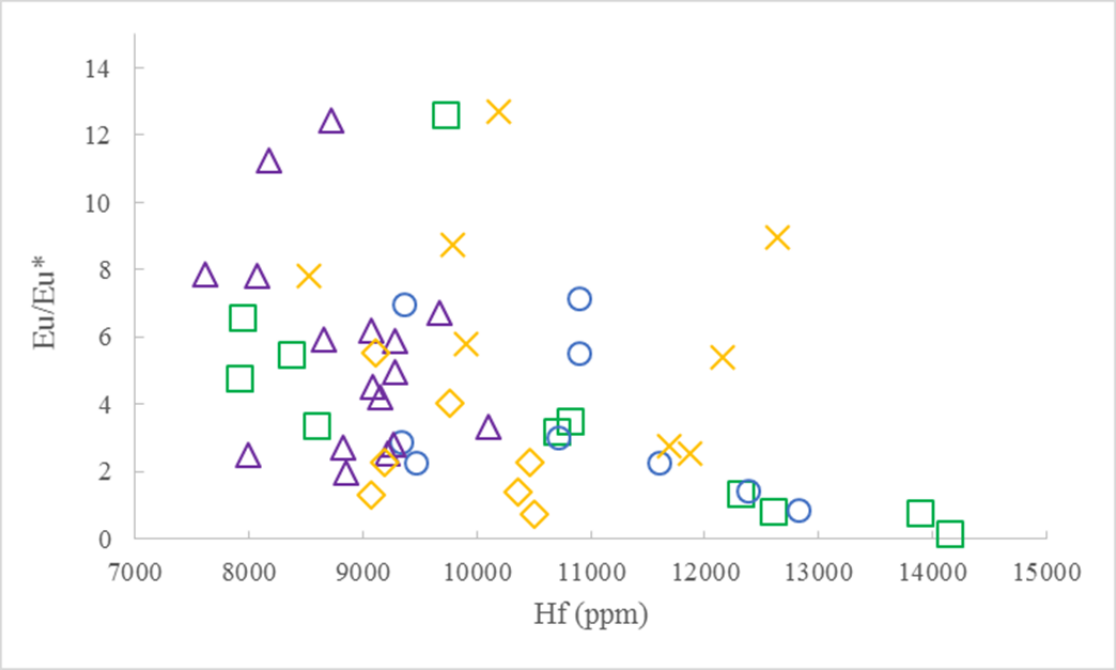

Figure 9. Eu/Eu* vs. Hf (ppm) as a proxy for feldspar fractionation, symbology is same as previous figures.

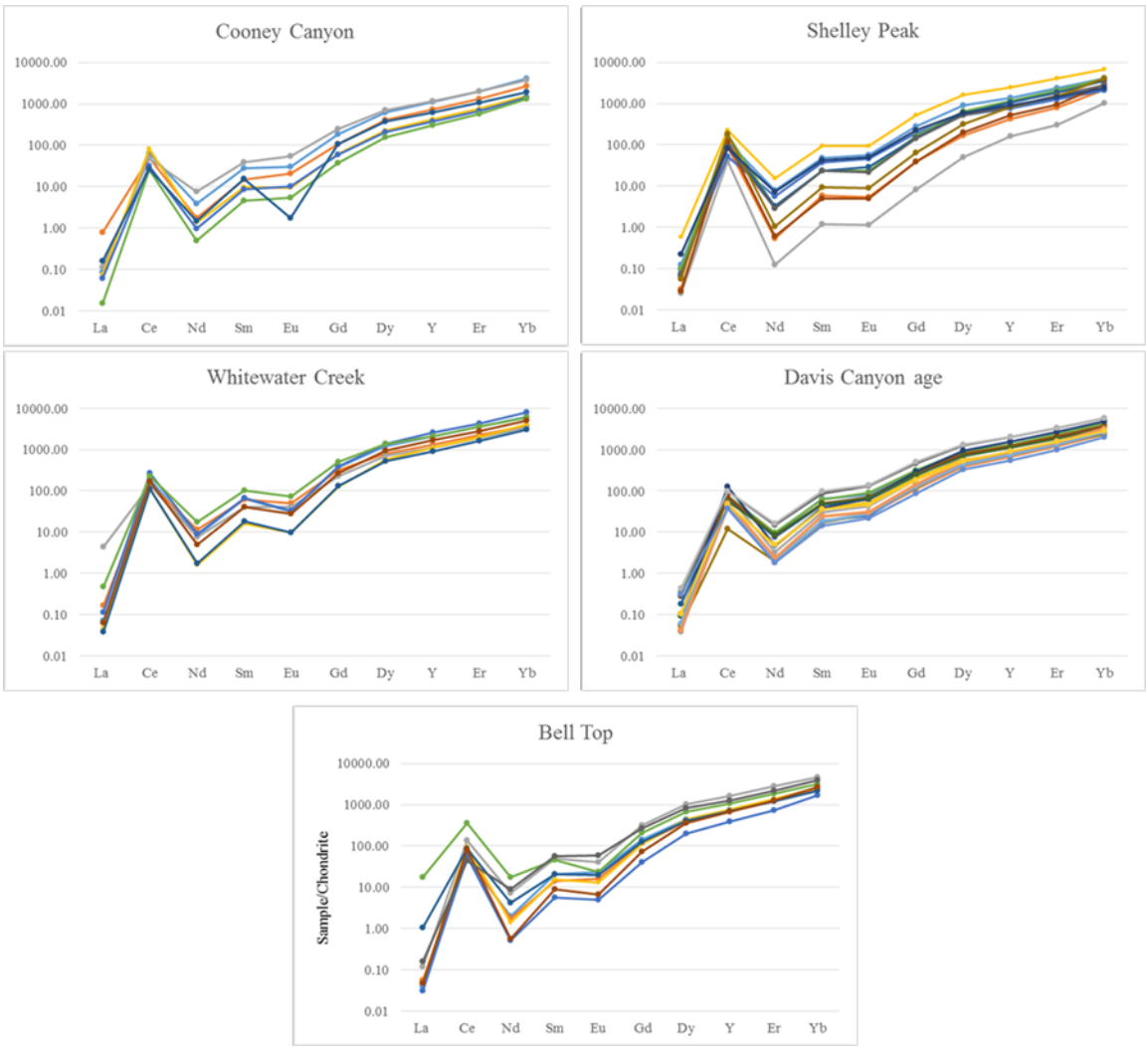

Figure 10. Chondrite-normalized REE from zircon plots for all study units. Chondrite values are from Wasson (1985).

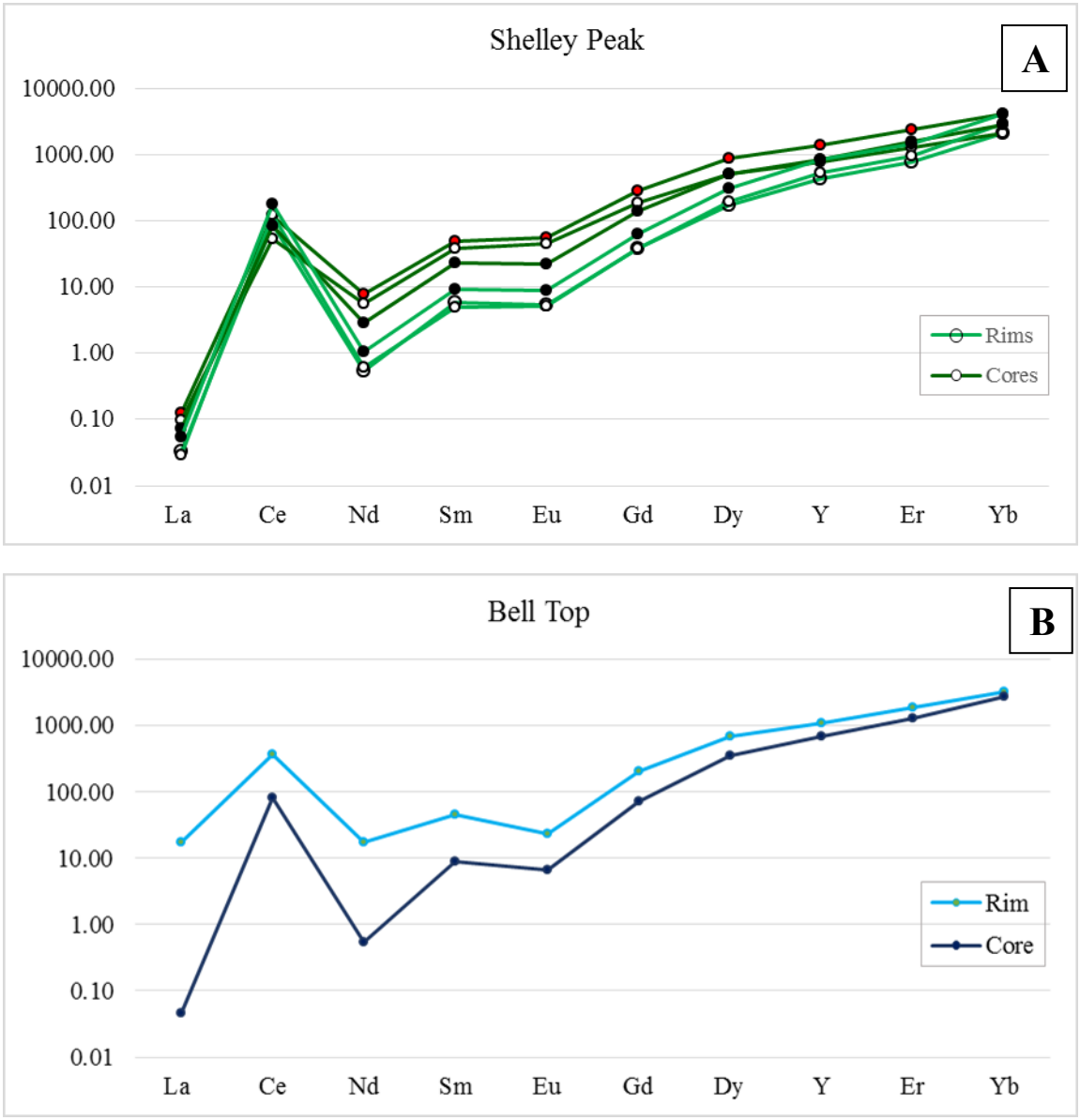

Figure 11. A) Rim vs. core REE analyses results for 180-SP-1. B) Rim vs. core analyses results for UV-R2. The dark green trend lines are core analyses, and the light green lines are rim analyses. The symbols correspond between core and rim on a single grain.

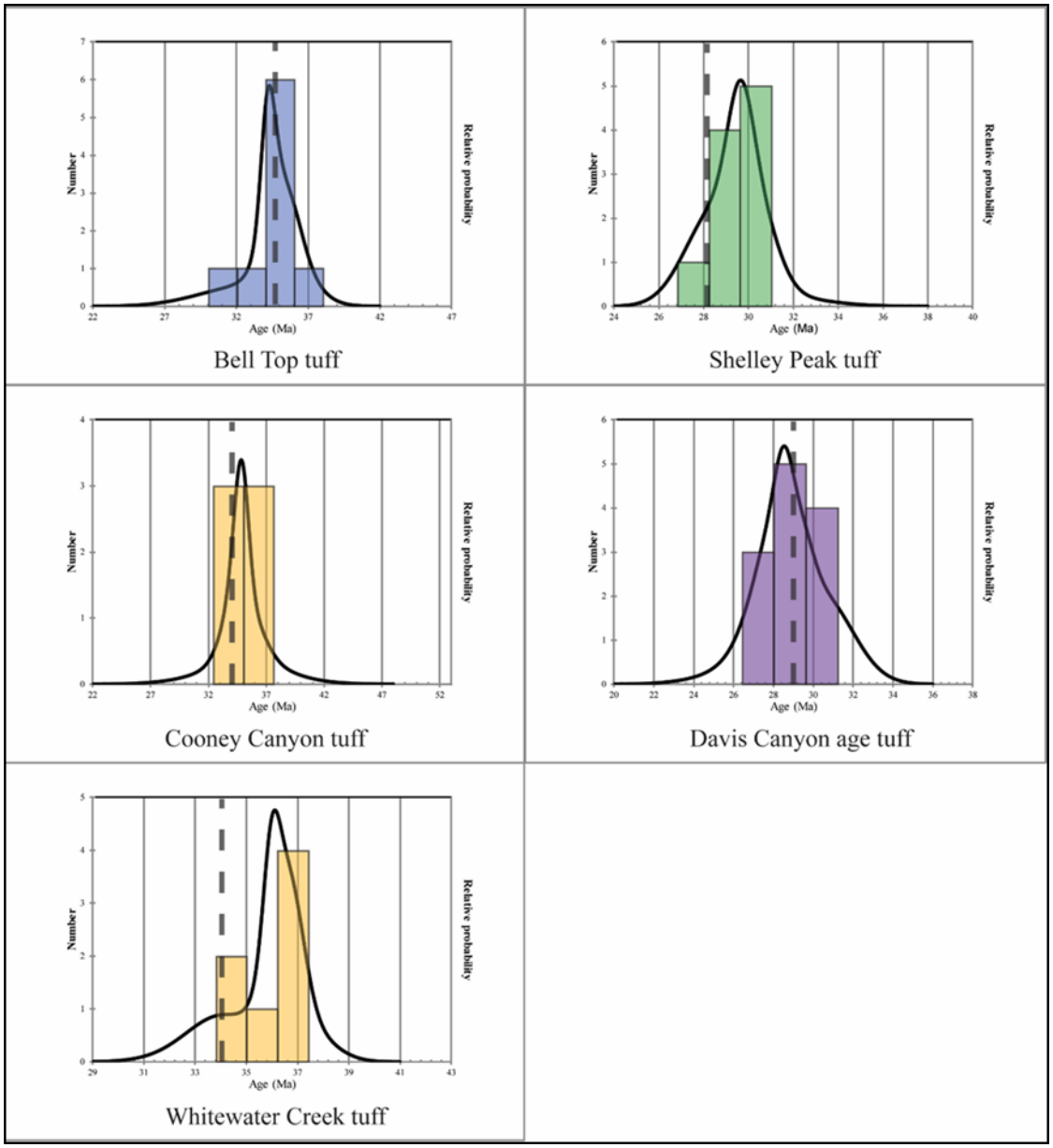

Figure 12. Probability density function curves for zircon age dates. The dashed bold line is the 40Ar/39Ar eruption age from McIntosh et al. (1992).

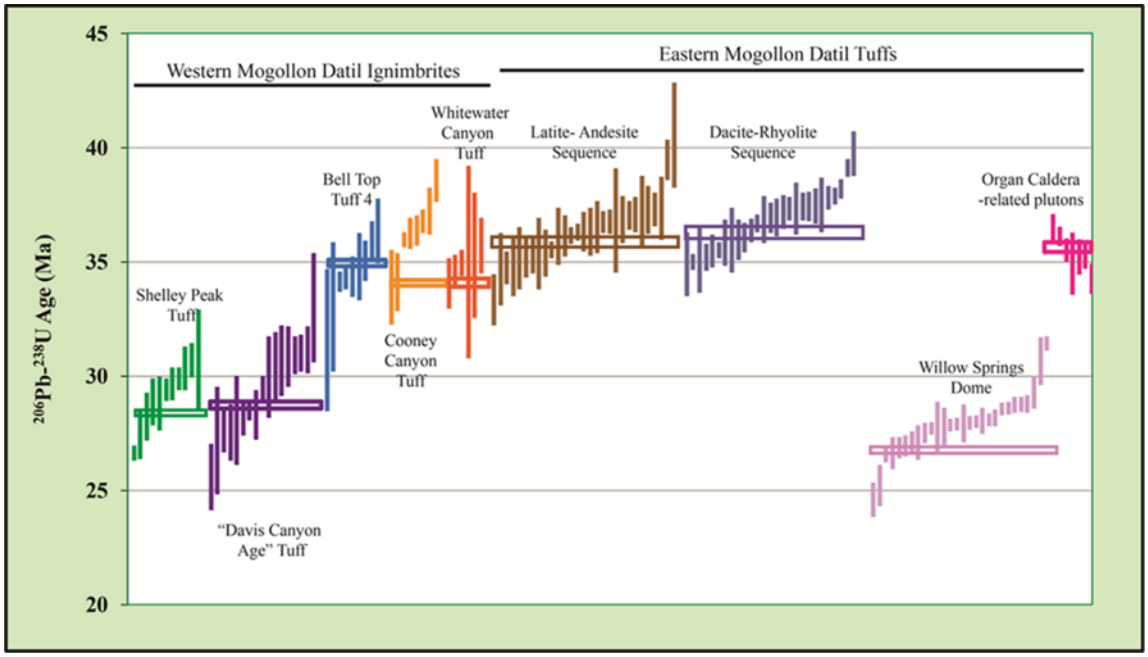

Figure 13. U-Pb ages with $^{40}Ar/^{39}Ar$ eruption date crossbars (McIntosh et al., 1992). The length of each individual bar is ±1σ internal uncertainty. Eastern MDVF data from Michelfelder and McMillan, 2012. Organ Caldera data from Zimmerer and McIntosh, 2013.